
**Maisterintutkielma / Magisteravhandling /
Master's thesis**

**Solid Earth Geophysics**

# Simulation of space weathering on asteroid spectra through hydrogen ion and laser irradiation of meteorites

Lakshika Palamakumbure

2022

Tomáš Kohout, University of Helsinki
Ilmo Kukkonen, University of Helsinki
Kateřina Chrbolková, University of Helsinki, and Charles University, Czech Republic

Geologian ja geofysiikan maisteriohjelma / Magisterprogram i geologi och geofysik /
Master's Programme in Geology and Geophysics

Matemaattis-luonnontieteellinen tiedekunta / Matematisk-naturvetenskapliga fakulteten / Faculty of Science

HELSINGIN YLIOPISTO
HELSINGFORS UNIVERSITET
UNIVERSITY OF HELSINKI
MATEMAATTIS-LUONNONTIETEELLINEN TIEDEKUNTA
MATEMATISK-NATURVETENSKAPLIGA FAKULTETEN
FACULTY OF SCIENCE

| Tiedekunta – Fakultet – Faculty<br>Faculty of Science | Koulutusohjelma – Utbildningsprogram – Degree programme:<br>Master's Programme in Geology and Geophysics |
|---|---|

Opintosuunta – Studieinrikting – Study track: Solid Earth Geophysics

Tekijä – Författare – Author: Lakshika Palamakumbure

Työn nimi – Arbetets titel – Title: Simulation of space weathering on asteroid spectra through hydrogen ion and laser irradiation of meteorites

| Työn laji – Arbetets art – Level: Masters | Aika – Datum – Month and year: May 2022 | Sivumäärä – Sidoantal – Number of pages: 48 |
|---|---|---|

Tiivistelmä – Referat – Abstract

Space weathering can be defined as the combination of physical and chemical changes that occur in material exposed to an interplanetary environment on the surface of airless bodies. This process produces amorphous surface layers often containing small opaque particles such as nanophase metallic iron ($npFe^0$). This darkens the topmost layer resulting in alterations in material spectroscopic features.Eventually it can lead to misinterpretation of remotely sensed data in the visible- near-infrared (VIS-NIR) spectrum. The goal of this research is to simulate solar wind effects on asteroid spectra through low energy 1 keV hydrogen ion irradiation of meteorite powder samples and measure the changes in their reflectance spectra. This allows to understand how space weathering depends on the mineralogy of the material. We used Bjurböle (L/LL4), Avanhandava (H6) and Luotolax (Howardite) meteorites. $H^+$ ion irradiation was carried out on powdered samples compressed into pellets. The pellets were placed into a vacuum chamber with pressure between $1.2 \times 10^{-7}$-$2.4 \times 10^{-7}$ mbar for the whole experiment. To simulate solar wind irradiation, $H^+$ ions were used with 1 keV under three fluences; $1 \times 10^{17}$, $2 \times 10^{17}$ and $5 \times 10^{17}$ ions/cm$^2$. Subsequently reflectance spectra of the samples were measured and processes using Modified Gaussian Model (MGM) to derive key spectral parameters.

Both chondrites show significant reddening in the VIS region. Bjurböle being an LL, it is more oxidized than Avanhandava. The reddening in the NIR region is more significant in Avanhandava than in Bjurböle. My work indicates that even for low-energy solar wind conditions, the chondritic materials (Q/S-type asteroids) with high olivine content and/or higher fayalite (Fa) compositions are more susceptible to silicate absorption bands reduction. Luotolax meteorite being howardite rich in orthopyroxene and clinopyroxene, shows VIS reddening but not observable band depth changes with increasing exposure to $H^+$ ion irradiation. The smaller change in Luotolax may be due to higher pyroxene resistance to low-energy ion irradiation. Overall, at short timescales and typical solar wind energies, VIS slope reddening is the most dominant factor in all three material compositions.

Avainsanat – Nyckelord – Keywords Space weathering, low energy hydrogen ion irradiation, howardite, ordinary chondrites

Säilytyspaikka – Förvaringställe – Where deposited

Muita tietoja – Övriga uppgifter – Additional information

**CONTENTS**

## 1. INTRODUCTION

Space weathering plays a significant role in interpreting remotely sensed data of asteroid surfaces because it causes alterations in asteroid surfaces physical and optical properties (Hapke 2001, Marchi et al. 2005). The optical properties of an asteroid get affected by the formation of nanophase iron particles, for example, on regolith grains (Pieters et al. 2000) by three main space weathering agents, micrometeorites impacts, solar wind, and galactic radiation. More than 99% of the solar wind consists of hydrogen and helium ions with uniform broad velocity distribution (Gosling 2007). This research simulates the solar wind component of space weathering on asteroid spectra through hydrogen ion irradiation of meteorite powder samples and evaluates the changes in their reflectance spectra.

The study of asteroids is of interest to the scientific and industrial community for several reasons. Asteroids are considered the remnants of debris from the inner solar system formation process and Earth's biosphere formation process (Yeomans 1998). It is widely believed that they provide key information on the composition of the Solar System and its formation (NASA, Fernandez et al. 2015, Pfalzner et al. 2015). Also, asteroid mining has been identified as a viable long-term solution to obtain certain rare metals, which now have attracted the attention of the industrial community (MIT 2016, Williams 2020). Hence, it is important to identify asteroids' composition and physical and chemical properties.

For decades, remotely sensed ground-based observations have been carried out to identify the physical characteristics and chemical composition of not only asteroids but also of other planetary bodies such as the Moon (Fernandez et al. 2015). These observations were carried out using visible/near-infrared (VIS/NIR) and mid-IR (MIR) spectra. In the last decade, the studies expanded with a series of successful spacecraft missions, which were able to collect samples from near-Earth asteroids (162173) Ryugu, (25143) Itokawa, and the Apollo mission from the Moon (Tachibana et al. 2014, Fernandez et al. 2015, Reddy et al. 2015). There was a significant mismatch between the optical properties of the interior of the collected samples and reflectance spectra obtained via ground-based observations (McCord and Johnson 1970, McCord and Adams 1973). The reason behind this mismatch was identified as the effect (see Figure 1**)** of space weathering (McCord

and Adams 1973, Pieters et al. 1993, Hapke 2001). Such mismatches between the remotely sensed spectra and actual spectra caused by space weathering increase the challenge of linking the meteorites with their parent body or their source body. Hence, understanding space weathering is important for the correct interpretation of the chemical composition of asteroids using remotely sensed spectral data (Clark et al. 2002).

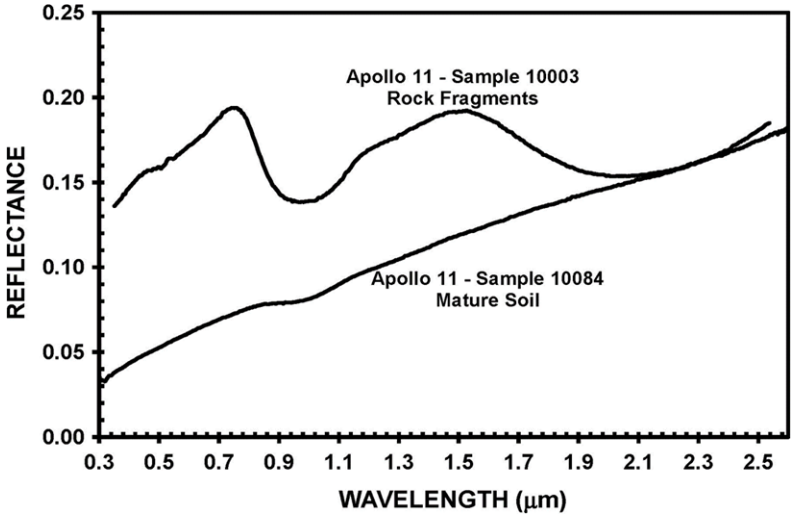


Figure 1. This figure illustrates the spectral mismatch between the lunar rock fragments and lunar mature soil. Spectra of lunar mature soil indicate darkening in albedo, reddening in slope and reduction in intensity of silicate absorption bands relative to the spectra of rock fragments (Adams and Jones 1970).

Previous research has proven that space weathering occurs on airless bodies (Chapman 1996, Pieters et al. 2000, Hapke 2001, Bennett et al. 2013, Pieters and Noble 2016). However, the degree of the mismatch between asteroid reflectance spectra and meteorite reflectance spectra is not coherent. For example, comparing ordinary chondrite spectra to that of compositionally similar S- type asteroids, space weathering features in spectra include albedo decrease, slope redding, and decrease in band depth (Clark et al. 2002). However, reflectance spectra of Howardite-Eucrite-Diogenite (HED) with asteroid (4) Vesta has a better match (McCord et al. 1970, McSween et al. 2013). Therefore, the remaining question is not whether space weathering occurs on an asteroid resulting in alteration in the spectra, but why there are different degrees of space weathering occurring on asteroids.

The goal of this research is to simulate solar wind effects on asteroid spectra through low energy hydrogen ion irradiation of meteorite powder samples to determine spectral changes due to typical solar wind energies. Many studies carried out before have used high-energy ion irradiation using ions such as $Ar^+$ and $He^+$ with energy levels of over 4 - 10 keV. But the typical solar wind with $H^+$ has low energy, around 1 keV. Hence this study will observe how reflectance spectra change under ion irradiation conditions closer to solar wind conditions. Ion irradiation was carried out at the Helsinki Accelerator Laboratory, Finland. Studies have shown that in certain experimental conditions, pyroxene does not alter the spectra under helium and argon ions irradiation but shows a significant change with hydrogen irradiation (Marchi et al. 2005, Chrbolková et al. 2021). This study will facilitate re-examining how to remove space weathering effects simulated under a more realistic environment from the spectrum. Another objective is to study the response of meteorites with different compositions to space weathering simulations.

The study hypotheses that different minerals may respond differently at low solar wind energies and low fluences, in other words, short time scales. Thus, the initial space weathering effect on reflectance spectra may differ on various bodies of distinct composition. At a longer time scale, close to space weathering saturation, the change may become similar.

To achieve the goals and test the hypothesis, three different meteorites were used: ordinary chondrites Bjurböle (L/LL4), Avanhandava (H6), and achondrite Luotolax (Howardite). Powdered meteorite pellets were created and irradiated with 1 keV, $H^+$ ions under three fluence steps to simulate three exposure times: $2.17 \times 10^{17}$ $H^+/cm^2$, $5.4 \times 10^{17}$ $H^+/cm^2$, $1.37 \times 10^{18}$ $H^+/cm^2$ to simulate solar wind irradiation at different time scales. The use of pellets with powdered samples has been shown to have effective and representative results by Chrbolková et al. (2021). This method also has been used and proven in the work of Brunetto et al. (2014). Exposure time was calculated based on the flux of protons at approximately 1 au, and the time scale corresponding to our fluences is less than 1000 years. The reflectance spectral measurements in the VIS-NIR wavelength range were carried out at the Department of Physics, the University of Helsinki, using a Spectro-radiometric measurement system. Individual mineral absorption bands from the spectra were deconvolved using the Modified Gaussian Model (MGM),

which has been identified as an accurate mathematical description of the shape of isolated electronic transition absorption bands (Sunshine and Pieters 1993).

The findings of this research will contribute to the ESA project related to the Hera CubeSat and Comet Interceptor mission (MIRMIS payload) to interpret the hyperspectral images of asteroids or comets.

# 2. **BACKGROUND**

## 2.1. Classification of meteorites

There are different types of meteorites. More than 50,000 meteorites have been discovered on Earth (NASA). These meteorites have been categorized based on mineralogical and petrographic characteristics and their whole-rock chemical and O-isotopic composition. The meteorite classification system has evolved over the last two centuries, starting from 1860 with G. Rose's classification. The classification system used for this study is based on Prior (1920) and Mason (1967), which has been modified with modern studies.

The name of the meteorite is based on the location in which it is found, and if they are found in a desert region, they are given a number. If the fall of a meteorite is observed during a recorded fall event, they are considered a 'fall,' and if not, they are considered a 'find.' Fall meteorites are considered less weathered in the Earth's environmental conditions and the weathering level is W0. 'Find' meteorites are considered more exposed to Earth's environmental conditions because the fall date is unknown. In this scenario, the weathering level is denoted W1 or higher and can be expected to some alteration in the chemical and mineral (e.g., oxidation and aqueous alteration) and in physical condition (e.g., plugging of pores with weathering products) of the meteorite.

In modern meteorite taxonomy, meteorites have been divided into two major classes, chondrites, and achondrites (Kallemeyn 1996). The chondrite class is divided into two super clans named carbonaceous and non-carbonaceous. The non-carbonaceous super clan includes ordinary chondrites (OCs), Rumuruti (R), and Enstatite (E). Clans are grouped based on the similarities in lithophile-element abundant, O-isotopic mixing line, isotopic anomaly, and/or based on petrologic characteristics. Complete meteorite taxonomy is given in Appendix 1.

Groups within OCs are H, L, and LL, which have overlapping properties in petrologic characteristics and O-isotopic composition (Weisberg et al. 2006). OCs consists of millimeter-sized chondrules with various textures and minerals. They are dominated by olivine and orthopyroxene (low Ca). The difference between H, L, and LL groups is their

oxidation state (i.e., the ratio of metallic Fe ($Fe^0$) to oxidized $Fe^{2+}$ (FeO) in silicates. H chondrites have the highest $Fe^0$/FeO ratios (lower fayalite (Fa) and ferrosilite (Fs) component in silicates) and thus, are more reduced. Metal iron content in H chondrites by weight is between 25% to 28%. On the contrary, LL chondrites are more oxidized and have the lowest total iron metal and highest iron oxide content in silicates. The iron percentage in LL chondrites by weight is between 19% to 22%. L chondrites are in their oxidation level in-between H and LL.

Achondrites are differentiated bodies after melting minerals and metal, destroying chondrules. HED (Howardite, Eucrite, Diogenite) are differentiated basaltic achondrites that has different elements and element ratios than terrestrial basalts (Ahrens and Danchin 1971), and many are impact-produced monomictic or polymictic breccias. As shown in Figure 2, eucrites are thought to originate in the crust of (4) Vesta and are Ca- and Fe-rich compositions (Burbine et al. 2009). Unlike eucrite, diogenite is thought to be originated deep under the crust with a more Mg-rich and Fe-poor composition. Howardite is a cemented impact breccia of eucrite and diogenite clasts. The main mineral composition of howardite is orthopyroxene and Na-poor plagioclase (Duffard et al. 2006, Meteoritical Bulletin Database 2022). Average petrological characteristics of the OCs group and HED clan are summarised in Table 1.

Table 1. Average petrological characteristics of OC group (Modified after Weisberg et al. (2006))

| | H | L | LL | HED |
|---|---|---|---|---|
| Chondrule abundance (vol%) | 60-80 | 60-80 | 60-80 | - |
| Matrix abundance (vol%) | 10-15 | 10-15 | 10-15 | - |
| CAI – AOA abundance (vol%) | <<1 | <<1 | <<1 | - |
| Metal abundance (vol%) | 8 | 4 | 2 | rare |
| Average chondrule diameter (mm) | 0.3 | 0.7 | 0.9 | |
| Olivine composition (mol% Fa) | (16-20)¤<br>19.3** | (23-26)¤<br>25.2** | (27-32)¤<br>31.3** | 27-44 |
| Low-Ca pyroxene Fs (mol%) | - | - | - | 14-79 |
| Plagioclase An (mol%) | - | - | - | 73-96 |

¤Range of compositions.
**Data for equilibrated verities

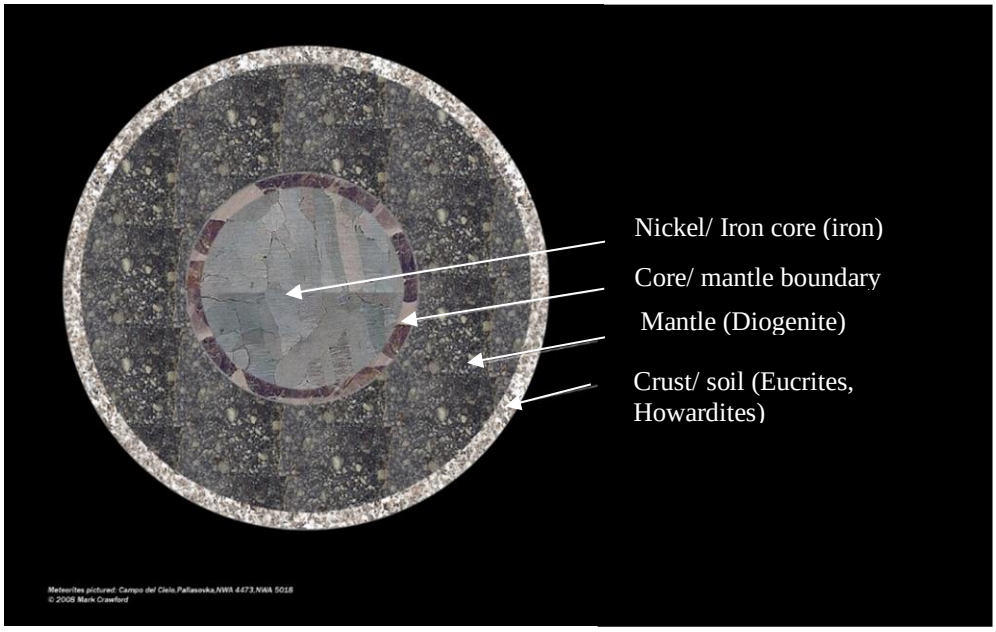


Figure 2. A model of a differentiated parent body illustrating the origin of some meteorites (modified from Crawford (2008))

Chondrites can also be categorized according to petrologic type, as shown in Figure 3 (Van Schmus and Wood 1967). This categorization uses numbers where the value varies according to the increase in the degree of aqueous alteration and increase in the degree of thermal metamorphism. Petrographic type 3 chondrites are the least altered. Petrographic types 1-2 are hydrothermally altered, while types 4-7 are progressively more thermally metamorphosed, with type 7 being completely recrystallized or melted chondrite. Some or most of these chondrites are impact melted. Nevertheless, this categorization does not prove for all the chondrites (Huss et al. 2006) as this does consider not only petrological observations but also the mineral composition and thermoluminescence properties of the meteorite. Hence, it is difficult for some meteorites, such as E chondrites, to distinguish between 3 and 4 as it considers the heterogeneity of olive and E chondrites has less olivine composition.

Another classification type of meteorites is by shock level. The shock classification system by Stöffler et al. (2018, 2019) is based on the degree of shock pressure they experienced. The shock level is determined based on the shock effects in olivine and plagioclase, such as recrystallization of olive and mechanical defects in the crystal lattice. For chondritic rocks, the progressive stage of shock metamorphism was denoted from C-S1 to C-S7. C-S1 represents the 'unshocked', and C-S5 to C-S7 stands for 'whole-rock melting'. Pressure conditions for each shock level are summarized inTable 2.

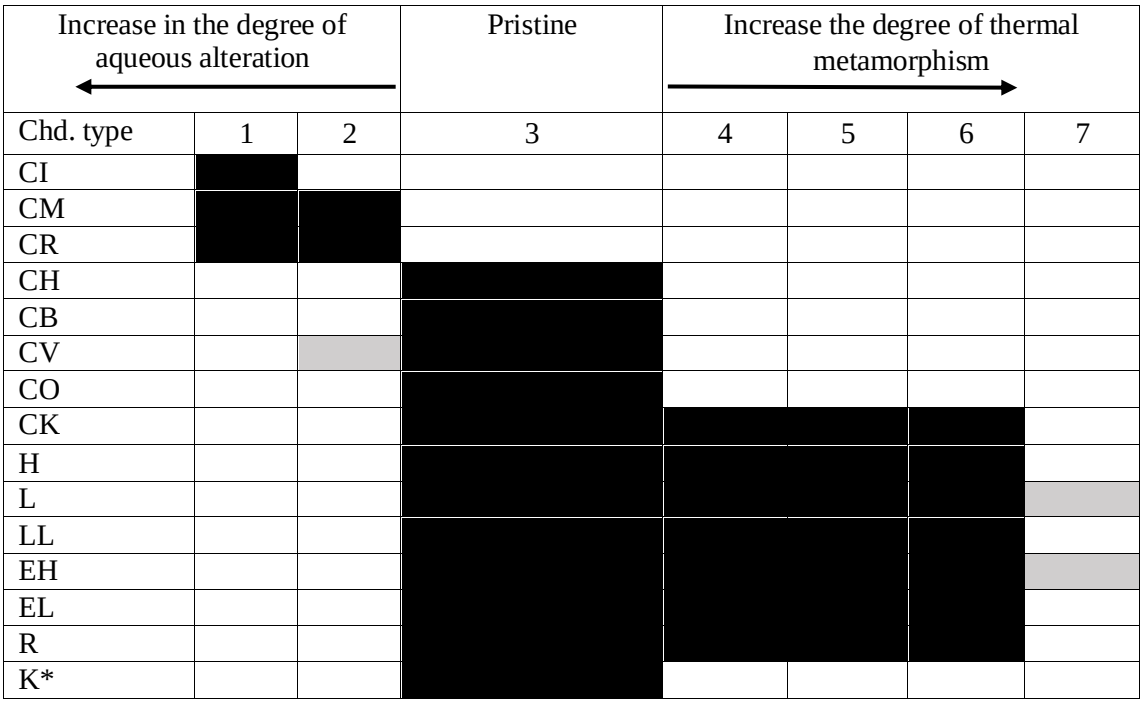


*Grouplet
Chd. = Chodrite group

Figure 3. Diagram showing the petrologic types for each chondrite group. (Weisberg et al. 2006)

Table 2. Pressure conditions for progressive stages of shock metamorphism for chondrites (modified after Stöffler et.al. (1991, 2019) and Schmitt (2000)).

| Shock stage | Transition pressure (GPa) | Effects resulting from equilibration peak shock pressure in olivine |
|---|---|---|
| C-S1 | | |
| | <4-5 | |
| C-S2 | | Undulatory extinction, Irregular fracture |
| | 5-10 | |
| C-S3 | | pf, Undulatory extinction, Irregular fracture |
| | 10-20 | |
| C-S4 | | Mosaicism (weak), pf |
| | 25-35 | |
| C-S5 | | Mosaicism (strong), pf and pdf |
| | 45-60 | |
| C-S6 | | Melting (re)crystallization and yellow-brown staining |
| | >70-75 | |
| C-S7 | | Whole-rock melting |

pf: Planar fractures, pdf: planar deformation features

## 2.2. Reflectance spectra of minerals and asteroid – meteorite connection

Since direct composition measurement of asteroids has practical limitations, the mineralogy of asteroids was measured using the remotely sensed reflectance spectra. Reflectance spectra of material contain absorption bands in the VIS-NIR region that characterize the composition and the structure of the absorbing species (Burns 1970, Marfunin 1979).

When considering the silicate minerals, which are the dominant mineral in most common meteorites, OCs, two major absorption bands can be observed. Olivine features a complex-wide absorption centered at approximately 1 μm. This absorption band results from three deep overlapping absorptions (Burns 1970). According to Burns (1993), these overlapping absorption bands result from the crystal field transition of $Fe^{2+}$ ions situated in M1 and M2 sites within the olivine structure. Absorption bands at short and long wavelengths are assigned to $Fe^{2+}$ ions situated in the smaller center centric M1 site, while the absorption band in the middle is assigned to the crystal field transition of $Fe^{2+}$ ions situated in the acentric M2 site. Furthermore, with increasing iron content, the position of the 1 μm absorption band tends to move towards the longer wavelengths (Burns 1970a, Adam1975, Burns 1993).

Pyroxene can be identified by two characteristic absorption features approximately at 1 μm and 2 μm (Burns 1970, Adams 1974, 1975). These absorptions enable pyroxene identification on the surface of many solid bodies in the solar system. Burns (1970) explains that this is the result of spin-allowed electronic transitions of $Fe^{2+}$ in distorted M1 and M2 crystal field sites. It was revealed that the absorption feature of orthopyroxene occurs at the shorter wavelengths while the absorption feature of clinopyroxene occurs further toward longer wavelengths (Cloutis and Gaffey 1991). Pyroxene absorption bands show systematic variation with increasing iron and calcium concentrations from 0.9 μm to 1.05 μm and 1.80 μm to 2.30 μm, respectively (Adams 1974, Hanzen et al. 1978). Important spectral features in VIS, NIR, and FIR regions are summarised in Table 3.

Meteorites found on the Earth are derived from the primary parent body, which can be either an asteroid or a planetary body such as Mars or Moon. Also, these meteorites can be derived from a secondary parent body, such as shattered asteroids. The linkage between

the meteorites and their parent body, asteroids, in most cases, was made by the photographic observations of meteorite falls and by calculating orbit path, projecting their path to the asteroid belt. Also, the compositional similarities between the different classes of asteroids and meteorites were used to identify the linkage between the meteorite and its parent body (NASA).

Table 3. Spectral features in VIS and NIR.

| Substance | VIS (μm) | NIR (μm) |
|---|---|---|
| Olivine | 1.0 | |
| Pyroxene | 1.0 | 2.0 |
| Oxidized Fe in phyllosilicates | 0.7 | |
| Hydroxyl -OH | 1.4 | 2.7 |
| $H_2O$ | | 1.9, 2.9, 3.1 |
| Carbonates | | 1.7 – 2.7 |
| Si-O stretch fundamental | | |

For decades remotely sensed data were used to determine the composition of asteroids. Bus-DeMeo taxonomy (DeMeo et al. 2009) is an asteroid spectrum classification based on principal components analysis (PCA) of combined VIS and NIR spectral data (see Figure 4).

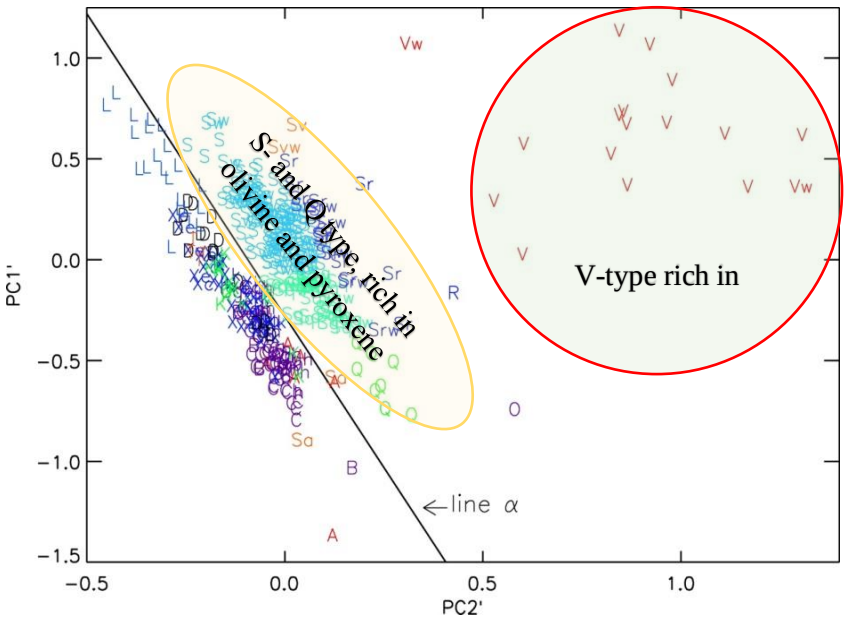


Figure 4. PCA of slope-corrected asteroid spectra, (Modified from DeMeo et al. (2009))

This taxonomy includes 25 classes. For example, S- and Q- type are siliceous or stony objects, A-types may have originated from a differentiated mantle, and V-types belong to (4) Vesta family. These were compared with the reflectance of meteorites to identify their parent body. However, the attempt to link the parent body and meteorites using spectral similarities was found challenging as no clear match was found between the most abundant class S-type meteorites and the ordinary chondrite group.

As mentioned in Section 2.1, OCs are dominated by olivine and pyroxene. Hence the reflectance spectra of OCs give absorption features at 1 and 2 µm. S- and Q- type asteroids exhibit diagnostic absorption features at 1 and 2 µm. Hence, OCs closely matched with S- and Q- type asteroid spectra with some deviations. As shown in Figure 5, reflectance spectra of OCs show similar mineralogy to S-type asteroids, but the slope does not match. Q-type asteroids are a closer match to OCs with a more similar slope than in the case of S-type. The difference between S- and Q-type spectra is that S-type has a steeper slope and are less bright than Q-type. Likewise, Bjurböle, being an OCs, has genetic relation to S- or Q-type asteroids (Clark et al. 2002, Binzel et al. 2004, Nakamura et al. 2011, Binzel et al. 2019). Avanhandava been an OCs, is also believed to be originated from S- or Q-type asteroids (Gaffey et al. 1993, Clark et al. 2002, Binzel et al. 2004, Binzel et al. 2019).

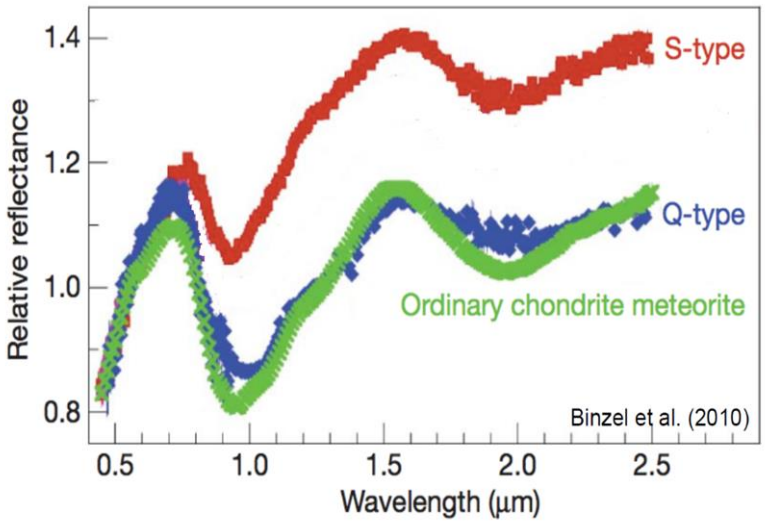


Figure 5. Reflectance spectra of OC, S- and Q- type asteroids (Modified from Binzel et al. (2010)).

HED are dominated by pyroxene. Hence the reflectance spectra of HED gives absorption features at 1 (narrow) and 2 µm (broad). V- type asteroids exhibit similar diagnostic absorption features at 1 and 2 µm. Hence, HED closely matched with V- type asteroid spectra, as shown in Figure 6. HED and V-type asteroid spectra have similar mineralogy, and slope but a slight shift in absorption features at 1 and 2 µm bands, as shown in Figure 6. Luotolax being howardite, has generic relations with V-type asteroids (McCord et al. 1970, Consolmagno and Drake 1977, Clark et al. 2002, McSween et al. 2013).

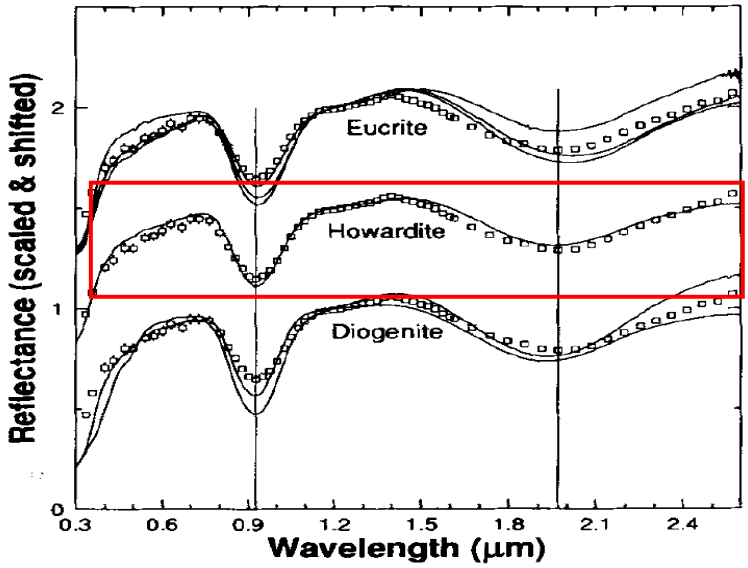


Figure 6. Reflectance spectrum of V-type asteroid (open squares) and HED meteorites (solid lines). Vertical solid lines are the centers of two major absorption bands of V-type asteroids. Red square indicates V-type spectral comparison with howardite (Modified from Hiroi et al. (1994))

### 2.3. Space weathering

After the return of lunar samples, scientists identified a miss-match between the reflectance spectra of fresh lunar soil and the reflectance spectra of the Moon. Hapke (2001) suggested that this is a result of space weathering. This led to discussions to consider space weathering also the reason behind spectral mismatch between asteroids and meteorites (Hapke 1973, Matson et al. 1977, Britt et al. 1992, Bell 1995a, 1995b). A similar observation was made with recent sample collections from (25143) Itokawa by Hayabusa (Tachibana et al. 2014).

The definition of space weathering is the combination of physical and chemical changes that occur to material exposed to an interplanetary environment on the surface of an airless body (Hapke 2001). The effect of the space weathering changes the mineral grains on the topmost layer with dislocations of the crystal lattice, blistering, surficial melting, sputtering, vaporization, and vapor redisposition (Fazio et al. 2017) (Figure 7). These space weathering processes produce small opaque particles such as nanophase iron ($npFe^0$) and optically active opaque (OAOpq) particles that darken the topmost layer resulting in alterations in their spectroscopic features. Three major space weathering alterations of the VIS-NIR spectra of bright bodies are usually observed: darkening (lowering the spectral albedo), reducing spectral contrast (dimming the strength of absorption features), and reddening the spectrum (increasing the slope of the continuum reflectance with increasing wavelength) (McCord and Adams 1973).

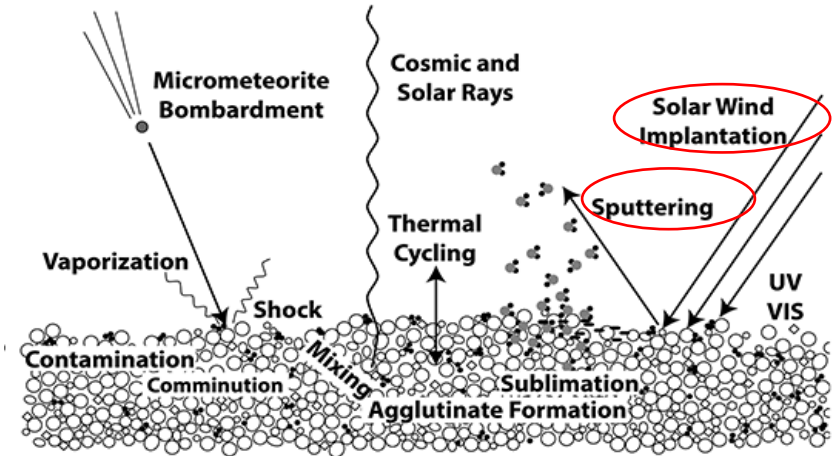


Figure 7. A summary of space weathering processes occurring on airless bodies. Red circle indicates the process related to solar wind irradiation (modified from Pieters and Noble (2016))

Among the three major space weathering agents, solar wind irradiation has been argued as the dominant mechanism for space weathering on asteroid surfaces. Interaction with solar wind ions changes the morphology of the surface by creating defects in the crystal lattice and removing atoms and molecules from the outermost layers (Crandall 2018). The surface of a body exposed to solar wind can be reduced to contain $Fe^0$ by simple chemical reduction of metal oxides by solar wind $H^+$ atoms implanted into mineral surfaces.

However, these weathering agents cause a spectral mismatch between meteorites and their parent bodies. Different meteorites give a different degree of spectral mismatch. For

example, when comparing ordinary chondrites to S- type asteroids, space weathering features in spectra includes all factors (albedo decrease, slope reddening, and decrease in band depth) with varying relative intensities (Gaffey et al. 1993, Clark et al. 2002). But while comparing reflectance spectra of HED meteorites with asteroid (4) Vesta, the dissimilarities show different general trends (McCord et al. 1970, McSween et al. 2013), such as the absence of reddening and absence of a decrease in albedo. But they do show a decrease in band depth. Some examples of linkage between the parent body with meteorites and the space weathering effects on reflectance spectral properties are illustrated in Table 4.

Table 4. Space weathering and asteroid type (Clark et al. 2002)

| Asteroid type | Meteorite Analogs | Mineralogy | Alteration Effect |
|---|---|---|---|
| S | H, L, LL chondrites; stony-irons, IAB irons, lodranites; inonites, siderophiles, ureilites | Olivine, pyroxene, metal | Albedo: up to 50% decrease<br>Red slope: weak to moderate increase<br>Band suppression: 50% decrease |
| V | Basaltic achondrites | Pyroxene, feldspar | Band suppression: 20% decrease |
| A | Brachinites, pallasites | Olivine | Red slope: moderate increase<br>Band suppression: 20% decrease |
| Q | H, L, LL chondrites | Olivine, pyroxene, metal | Albedo: 20–30% decrease<br>Band suppression: 20–30% decrease |
| Lunar | Lunar meteorites | Basalt, feldspar | Albedo: 50–75% decrease<br>Red slope: moderate to a strong increase<br>Band suppression: 50–75% decrease |

Many laboratory simulations of space weathering processes were conducted on meteorite samples, lunar soils, and rock samples in order to understand better the mechanisms involved. The solar wind was simulated by irradiating samples with ions ($H^+$, $He^+$, $Ar^+$) accelerated to different energies and with various fluences (Loeffler et al. 2009, Kuhlman et al. 2015).

In my thesis, I will focus on the solar wind component. Many studies carried out previously have used high-energy ions such as $Ar^+$ and $He^+$ with energy levels of over 4-10 keV. But the typical solar wind with $H^+$ has low energy, around 1 keV. Many attempts have been made to simulate more realistic environmental conditions to understand the effects of space weathering (Yamada et al. 1999, Sasaki et al. 2001, Clark et al. 2002, Sasaki et al. 2003, Fulvio et al. 2012, Hu and Lin 2012, Bennett et al. 2013, Kuhlman et al. 2015, Crandall 2018, Thompson et al. 2020, Chrbolková et al. 2021). Hence, Simulating the exact, realistic space weathering environmental conditions are yet to be improved. In my work, I used $H^+$ with 1keV energy which is more representative of a solar wind environment.

## 3. RESEARCH METHODS AND MATERIALS

To investigate solar weathering effects on different types of meteorites, $H^+$ ion irradiation was carried out on powdered samples compressed into pellets to simulate solar wind irradiation. Three types of meteorites were selected, namely, Avanhandava (H chondrite), Bjurböle (LL4 chondrites), and Luotolax (Howardite). The summarised methodology is shown in Figure 8 and discussed in detail below. Experimental conditions are described in detail from Sections 3.1 to 3.4.

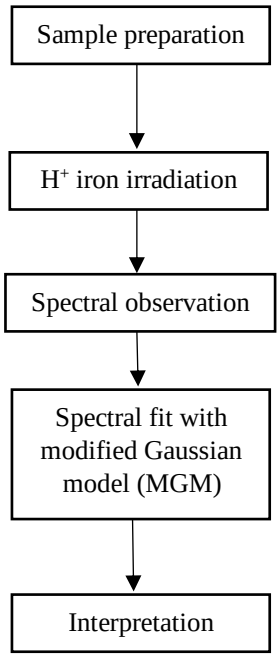


Figure 8. Summary of the methodology

### 3.1. Samples

In my research I used three meteorites: Bjurböle, Avanhandava, and Luotolax. Bjurböle is an L/LL4 OCs belonging to petrologic type 4 (Kallemeyn et al. 1989, Maksimova et al. 2021, Meteoritical Bulletin Database 2022). Its fall was observed in 1899. Bjurböle is of weathering grade W0 and shock level S1. Mineral modes in chondrules in Bjurböle mainly consist of olivine (~41 vol%), orthopyroxene (~30 vol%), feldspar (~12 vol%), and clinopyroxene (~6 vol%) (Kovach and Jones 2010). The studies carried out by Dodd et al. (1967) determined that the Fs is 20.7 mol% and Fa is 26.2 mol%. Bjurböle has

chondrules with a median diameter of $0.688 \pm 0.003$ mm, a mean density of $3.258 \pm 0.008$ g $cm^{-3,}$ and a median mass of $5.6 \times 10^{-4}$ g (Hughes 1977).

Avanhandava fall was observed in 1952. It is an H6 ordinary chondrite (Meteoritical Bulletin Database 2022) with a weathering grade of W0 and shock level S2. Mineral modes in chondrules in Avanhandava mainly consist of olivine (~35 vol%), orthopyroxene (~38 vol%), feldspar (~8 vol%), and clinopyroxene (~6 vol%) (Kovach and Jones 2010). Avanhandava is more reduced than Bjurböle, and Fa content is 17 mol%. Lewis and Jones (2022) have identified a peristerite intergrowth in the plagioclase, which indicates exsolution due to shock metamorphism.

Luotolax is recorded as an observed fall in 1803. It is a brecciated rock that falls under the category of howardite, an achondrite with weathering grade of W0. It is a brecciated rock with eucrite and howardite clasts as primary constituents. Eucrite clasts mainly consist of pyroxene and plagioclase intergrowths. Howardite clasts mainly consist of orthopyroxenes. Overall, Luotolax mainly consists of orthopyroxene and clinopyroxene (Fs~ 33-52), and plagioclase (Albite 4-19). (Meteoritical Bulletin Database 2022).

### 3.2. Sample preparation

Samples were obtained from the geology collections of the LUOMUS Finnish Museum of Natural History. The experiments were carried out with powdered samples pressed into pellets assuring a flat diffuse surface with a coherent textural consistency among all the samples. Approximately 600 mg from each meteorite were grounded using a mortar and pestle. The grounded powder of each sample was dry-sieved to a size less than 50 µm and homogenized to obtain a representative sample. Using the Specac manual hydraulic press (Figure 9), pellets were prepared at the University of Helsinki laboratory with a diameter of 13 mm and thickness of approximately 2.2 mm as described in Brunetto et al. (2014) and Chrbolková et al. (2021) using the following procedure.

Dehydrated KBr was used as an optically neutral substrate. First, 700 mg of KBr was pressed under 1 t for approximately five seconds using the hydraulic press. Then 100 mg of meteorite powder was added on top of the KBr pellet and pressed under 6 t for approximately six minutes to connect it with the substrate into the final pellet. KBr

substrate is optically neutral in the VIS-NIR region and guarantees higher durability of the pellet. Five pellets for each meteorite were created. These pellets are shown in Figure 10.

Figure 9. Left: Specac manual hydraulic press. Right: sample powder placed inside the sample holder.

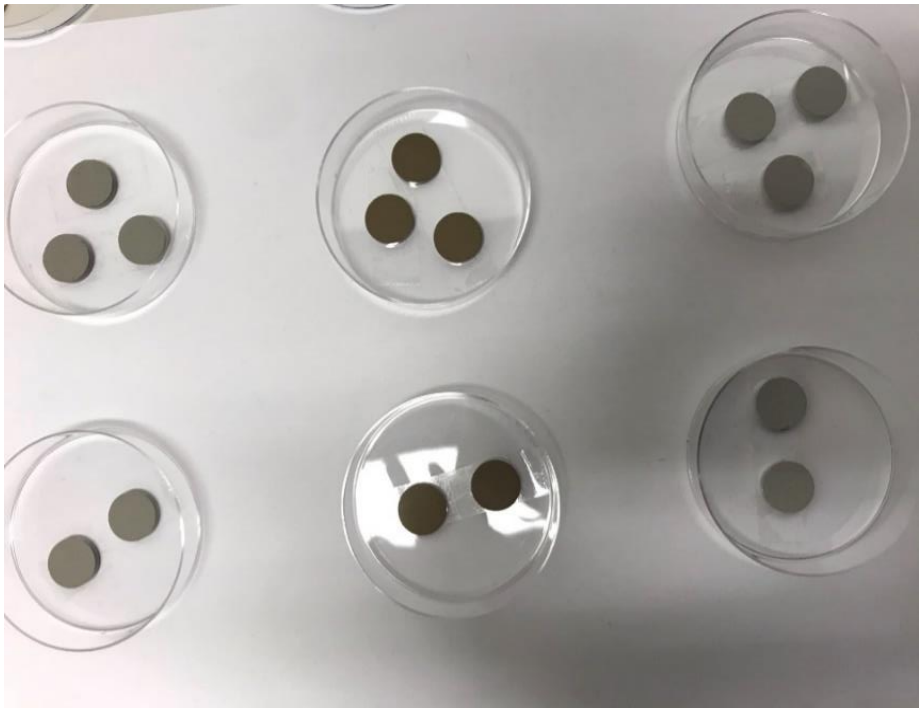

Figure 10. Prepared sample pellets. From left to right, Bjurböle, Avanhandava and Luotolax

### 3.3. $H^+$ ion irradiation

For ion irradiation, $H^+$ ions were used since they dominate the solar wind. To simulate the typical $H^+$ solar wind energies, the irradiations were conducted at the Helsinki Accelerator Laboratory. $H^+$ ions with 20 keV energy were decelerated down to 1 keV. The samples were irradiated using three fluences: $2.17 \times 10^{17}$ $H^+/cm^2$, $5.4 \times 10^{17}$ $H^+/cm^2$, and $1.37 \times 10^{18}$ $H^+/cm^2$, to simulate three different exposure times (Table 5). The sample mounted on the sample holder is shown in Figure 11.

Table 5. Irradiation fluences for samples

| Bjurböle | Avanhandava | Luotolax | Fluence ($H^+/cm^2$) |
|---|---|---|---|
| B1 | A1 | LU1 | $2.17 \times 10^{17}$ |
| B2 | A2 | LU2 | $5.40 \times 10^{17}$ |
| B3 | A3 | LU3 | $1.37 \times 10^{18}$ |

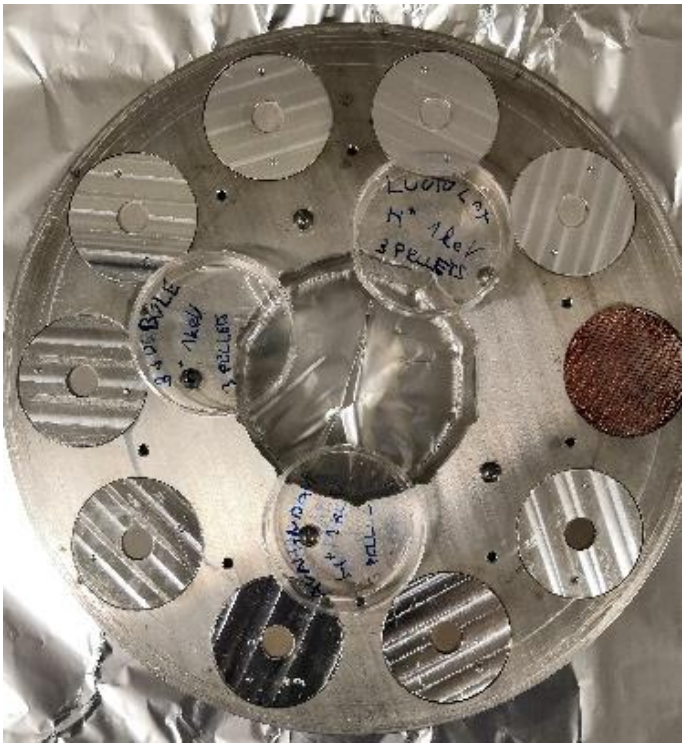

Figure 11: Sample mounted on the sample holder for ion irradiation experiment

During irradiations, the samples were placed in a vacuum chamber pressurized under approximately $1.2 \times 10^{-7}$ - $2.4 \times 10^{-7}$ mbar. After the simulation, samples were removed from the vacuum chamber for spectral analysis. According to Loeffler et al. (2009), after

the sample was taken out from the vacuum chamber in which the irradiation was taking place, rapid re-oxidation of the created metallic iron particles can occur. To prevents this, a surface passivation method described in Kohout et al. (2014) using a mixture of $N_2$ and 2 % of $O_2$ gas was carried out before extraction from the vacuum chamber.

### 3.4.Reflectance spectra measurements

The hemispherical reflectance VIS-NIR spectra were measured in the shortest possible time after the irradiations using an OL-750 automated spectro-radiometric measurement system by Gooch & Housego (Figure 12) situated at the Department of Physics, University of Helsinki.

Figure 12. OL-750 automated spectro-radiometric measurement system by Gooch & Housego at the Department of Physics, University of Helsinki

The OL-750 instrument is equipped with a polytetrafluoroethylene (PTFE) integrating spheres and a specular reflection trap. The spectra were measured relative to a PTFE (VIS)

standard and 5 mm slit with identical viewing geometry for all the segments of spectra. The incident angle was 10° to the surface normal, and the spectral resolution was between 5 and 10 nm. The spectrometer measuring parameters for different segments are summarised in Table 6.

Table 6. Measuring parameters and instrument configuration for different wavelength ranges

| Segment | 250 nm – 420 nm | 400 nm – 1100 nm | 1050 nm – 2500 nm |
|---|---|---|---|
| Measuring interval | 5 nm | 5 nm | 10 nm |
| Detector | PMT | Silicon | PbS |
| Sphere | PTFF | PTFF | PTFF |
| Lamp | Deuterium | Tungsten | Tungsten |

### 3.5. Data processing

Each reflectance spectra were consisting of three segments: segment 1 from 250 nm to 420 nm, segment 2 from 400 nm to 1100 nm, and segment 3 from 1050 nm to 2500 nm. Segments 1 and 2 have overlapping points from 400 nm to 420 nm, and segment 2 and 3 have overlapping points from 1050 nm to 1100 nm, and there was a shift between these overlapping points (Figure 13). These two spectral segments were connected by shifting the spectra using the difference between the mean values of overlapping points. The average value for overlapping points was calculated for each segment, and the difference between the two averages was calculated. Then the segment 1 and 3 were shifted relative to segment 2, adding the difference between the average values.

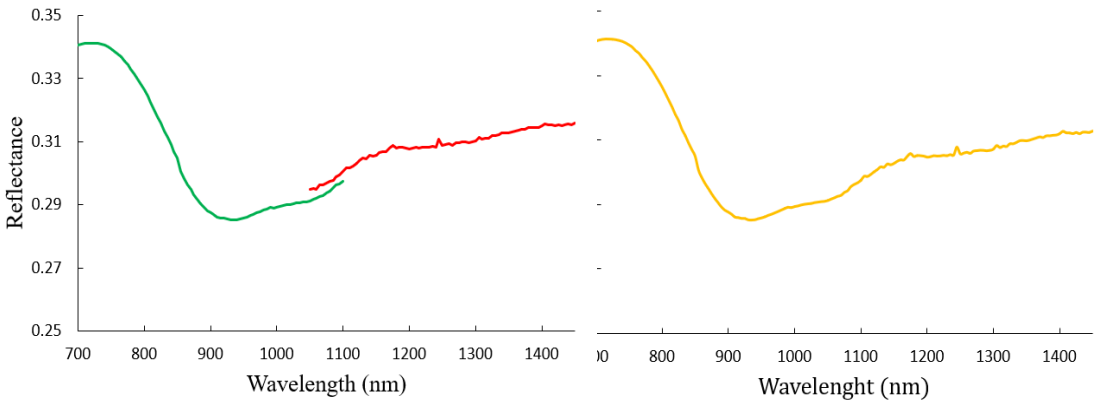


Figure 13. Figure on left gives segment 2 (green) and segment 3 (red) before the shift. Figure on right. Reflectance spectra after the connecting the two segments.

### *3.5.1. Spectral fits: Modified Gaussian Model*

Reflectance spectra of materials are often complex due to a combination of overlapping absorption bands. MGM is a spectral deconvolution algorithm to resolve individual absorption bands in complex spectra. Initially, Gaussian Model (GM) was used by many researchers such as Smith and Strens (1976), Clark and Roush (1984), Roush and Singer (1986). The GM was developed assuming that the absorption features observed in the VIS-NIR region are Gaussian-shaped absorption bands. This enables to deconvolve the reflectance spectra into absorption bands by fitting them with Gaussian distributions. For example, Singer (1981) shows that it is possible to represent 1 μm absorption band of olivine by three Gaussian distributions using the Gaussian model. This method allows extracting information from the measured spectrum without relying on the use of actual end members of spectral analogy. In 1990, Sunshine et al. developed the MGM with more accuracy when describing the shape of electronic transition absorptions. This model is capable of isolating absorption bands of common minerals such as olivine (Sunshine et al. 1990, Sunshine and Pieters 1993, Clénet et al. 2011), clinopyroxenes, and orthopyroxenes (Sunshine and Pieters 1993, Clénet et al. 2011).

MGM is widely used at present as it is an accepted mathematical description of the shape of isolated electronic transition absorption bands (Sunshine and Pieters 1993) described by a band strength, bandwidth, and band center. Band depth is the height from the minimum point to the continuum of a curve. Here the band strength is the band intensity in the natural logarithm of reflectance. Sunshine et al. (1990) explain that each absorption band can be represented by these three model parameters and two additional parameters; slope and an offset in the reflectance. Slope and offset represent the continuum where all absorption bands are superimposed onto. Such a continuum is a curved line at short wavelengths and a flat line at higher wavelengths (NIR). In this study, the modeling is carried out in a natural log reflectance, and all MGM fit spectra were given as a function of wavelength.

Han et al. (2020) carried out studies on MGM using olivine samples to diagnose spectral features to get insight into space weathering. They studied the effect of different continuum removal methods on the parameters of deconvoluted absorption bands. According to their studies, band center, shape, width, and strength depend on the different

descriptions of continua. Also, this study has shown that in logarithmic space, the second-order polynomial continuum can match the overall shape of the spectrum. Studies carried out by Sunshine and Pieters (1993) on natural and laboratory mixtures of pyroxenes conclude that the center and the bandwidths of primary absorption bands depend on end members and do not vary with modal abundance. Band centers, bandwidths, and relative band strengths also do not depend on particle size.

After the initial user input, the fit of the spectrum better than the specified RMS (in our case, $0.002\times 10^{-6}$) was obtained by the iterative optimization process. The second-order polynomial continuum fit was selected as it has been proven effective by Clénet et al. (2011) and Han et al. (2020).

Spectral parameters, namely the absorption band center, band strength, and full width at half maximum (FWHM), were obtained following the optimization. These parameters correspond to the amplitude of the MGM curve. In this study, each absorption band was labeled according to its respective band center.

*3.5.2. Spectral slope, band depth of 1µm region and 2 µm region calculation*

Spectral slope and overall band depth of 1 µm region and 2 µm region were determined manually using custom Octave code. Spectral slope at 1 µm and 2 µm regions were calculated as a linear fit connecting the local maxima of the 1 µm and 2 µm absorptions and depth as the distance between the linear continuum and local spectra minimum. An example is illustrated in Figure 14.

*3.5.3. Exposure time calculation*

$$Exposure\ time\ = \frac{Fluence\times 4}{2.9\times 10^{8}} \times \frac{1}{31.5792\times 10^{6}} \times \frac{1}{distance^{2}} \qquad (1)$$

The exposure time scale was calculated from the irradiated fluences based on the flux of protons at ~1 au by Schwenn (2000) and was used to determine the evolution of the spectral parameters as a function of the astrophysical timescale. The flux of the solar wind ions decreases approximately as a square of the distance from the Sun (Schwenn 2000).

According to Schwenn (2000), the flux of protons at 1 au is approximately $2.9 \times 10^8$ ions/ $cm^2$/ s. Exposure time in years was calculated using equation (1) by dividing the fluxes by the literature-based values. This was multiplied by the factor of four to approximate the object as a rotating sphere. The correction factor may vary according to the shape of the body. In this calculation, the body was considered a sphere. Calculated exposure times are given in Table 7.

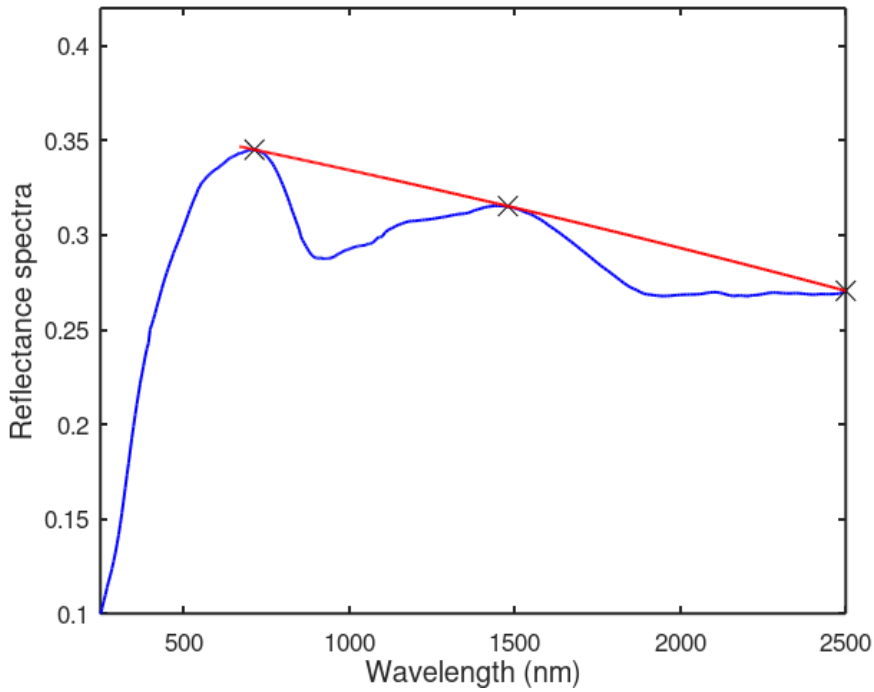


Figure 14. Blue: Reflectance spectra of Bjurböle. Red line gives the linear fit connecting the local maxima (×) of the 1 and 2 µm absorptions.

Table 7. Exposure time based on the irradiated fluence

| Fluences ($H^+/cm^2$) | Exposure time (yr) |
|---|---|
| $2.17 \times 10^{17}$ | ~93 |
| $5.40 \times 10^{17}$ | ~230 |
| $1.37 \times 10^{18}$ | ~590 |

# 4. RESULTS

This work simulated solar wind irradiation using $H^+$ ion with 1 keV as described in Section 3. Figure 15 shows the fresh samples and irradiated samples. There is an initial visual change in color between the fresh sample and irradiated samples, but not a significant difference between irradiated samples as fluence increases. The results of the irradiated spectra are given in Section 4.1.

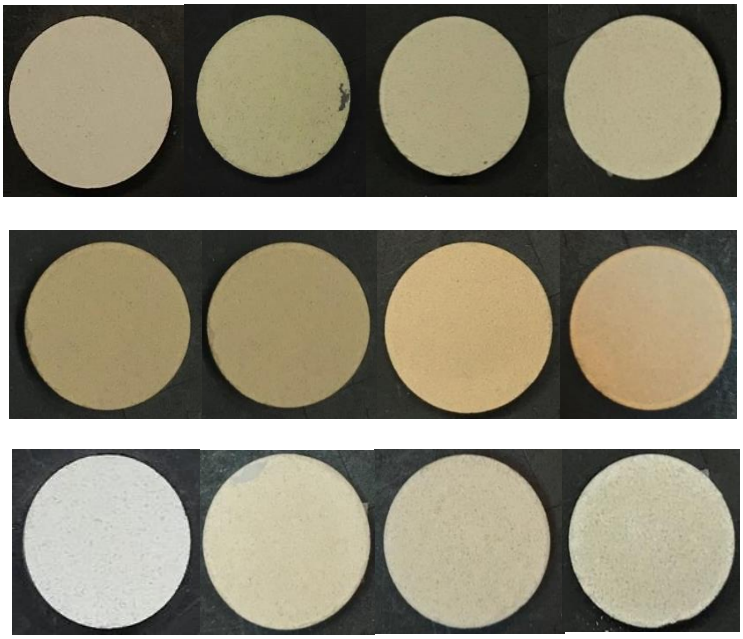

Figure 15. Fresh and irradiated samples. Fluence increases from left to right gradually; fresh, $2.17\times 10^{17}$ $H^+/cm^2$, $5.4 \times 10^{17}$ $H^+/cm^2$, $1.37 \times 10^{18}$ $H^+/cm^2$. Top: Bjurböle, middle: Avanhandava, bottom: Luotolax

## 4.1. Observed spectral changes resulting from the irradiation

Figure 16, Figure 17, and Figure 18 show the reflectance spectra for fresh and irradiated samples of Bjurböle, Avanhandava, and Luotolax, respectively. We can observe two major absorption bands at 1 and 2 μm in all meteorite samples. Overall, the slopes of the spectra are blue. That is due to the finely powdered nature of our samples. However, when comparing the relative slope evolution as a function of irradiation, the slope shows a relative reddening trend with increasing fluences. This is further illustrated in Section 4.2.

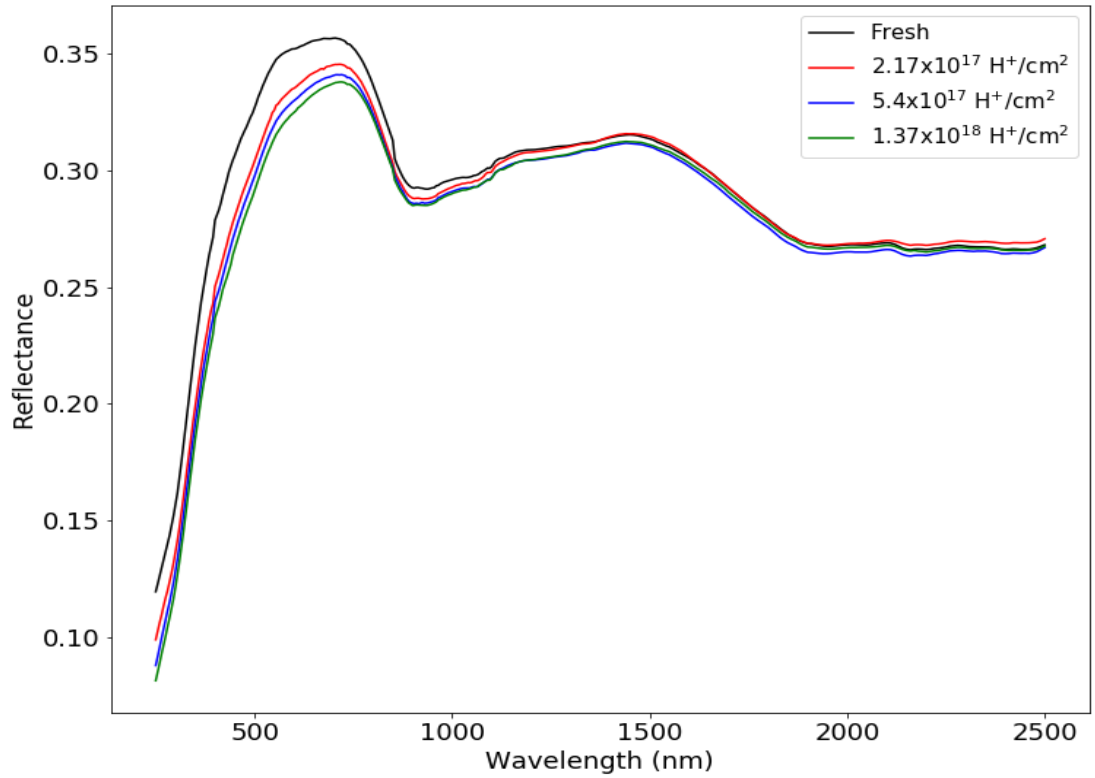


Figure 16. Reflectance spectra of fresh and irradiated samples of Bjurböle in VIS-NIR region

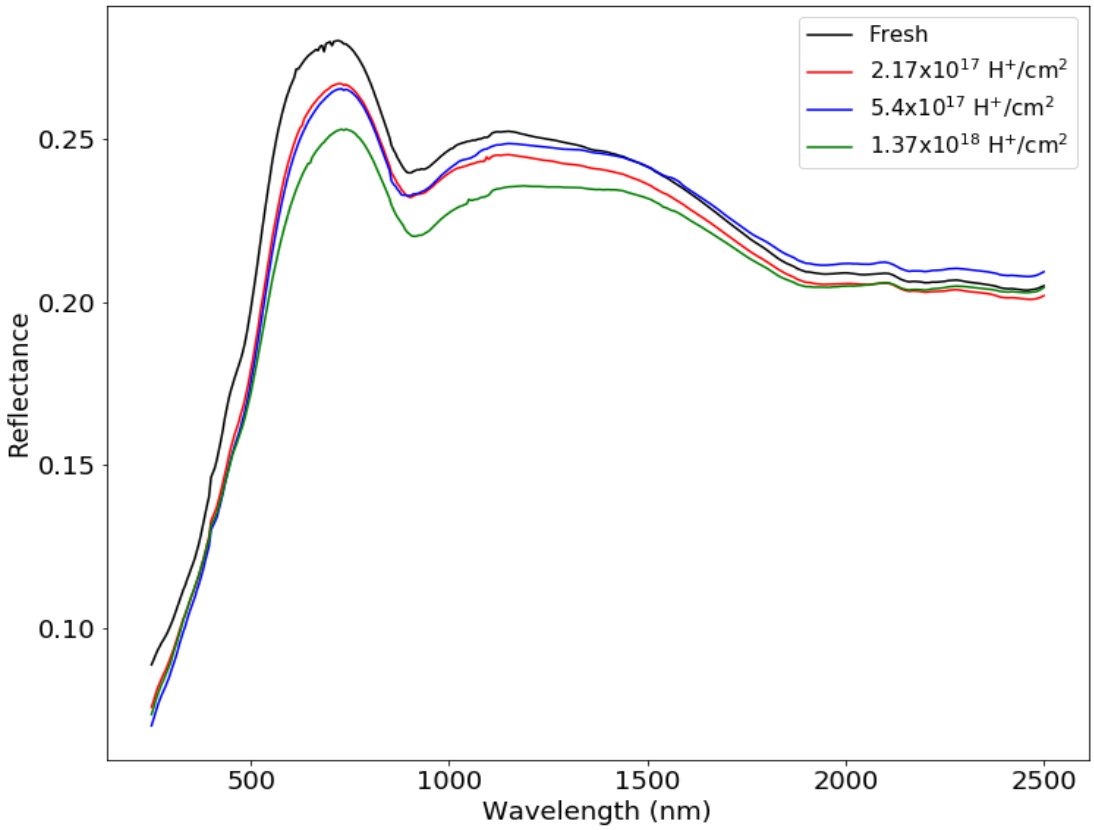


Figure 17. Reflectance spectra of fresh and irradiated samples of Avanhandava in VIS-NIR region

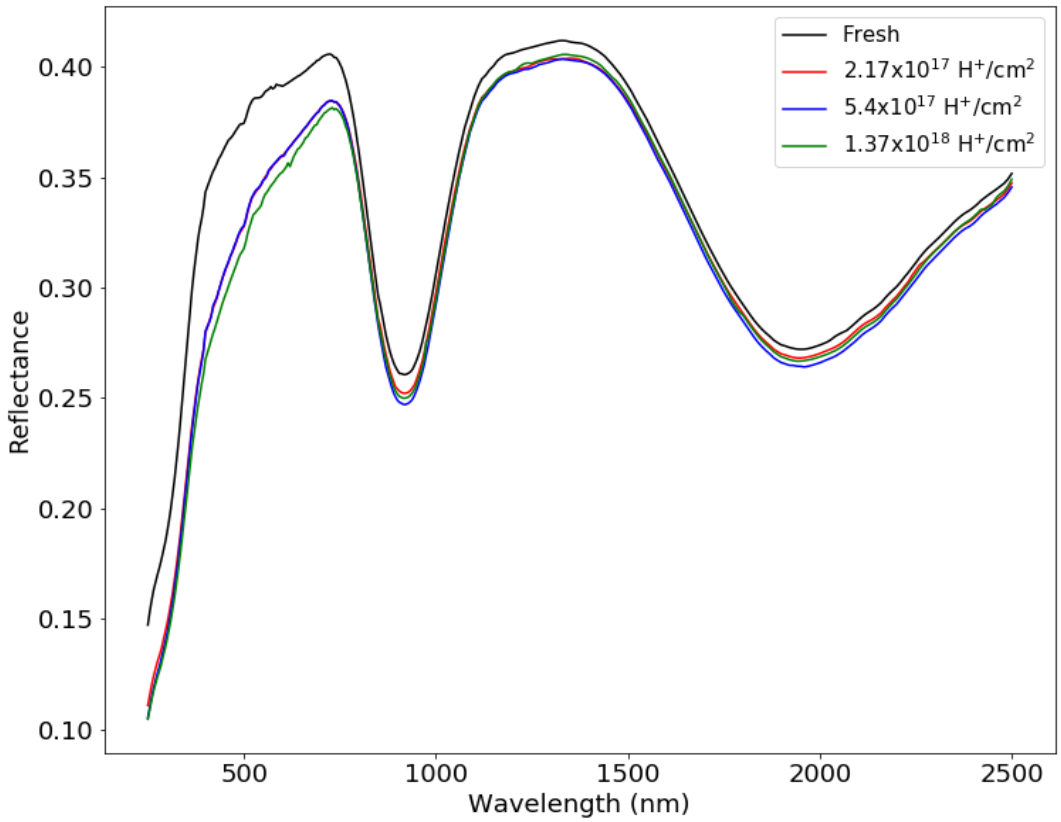


Figure 18. Reflectance spectra of fresh and irradiated samples of Luotolax in VIS- NIR region

### 4.2. Absorption band parameters

Figure 19, Figure 20, and Figure 21 give an example of MGM fits for Bjurböle, Avanhandava, and Luotolax, respectively. In all MGM models, the first two bands were used to obtain a better fit at the short wave drop in the spectra without further evaluation. For Bjurböle, six bands were the minimum number of bands to obtain the best fit. Bands 3, 4, 5, and 6 at 0.8 µm, 0.9 µm, 1 µm, and 1.9 µm were identified as the result of absorption by minerals. For Avanhandava, five bands were used to get the best fit, and bands 3, 4, and 5 at 0.9 µm, 1 µm, and 1.9 µm were identified as the result of mineral absorption. For Luotolax, five bands were used to get the best fit, and bands 3, 4, and 5 at 0.9 µm, 1 µm, and 1.9 µm were identified as the result of mineral absorption.

Changes in the band center, strength, and FWHM with increasing fluences were plotted against the exposure time given in Figure 21, Figure 22, and Figure 23 and Table 10. Calculated band slope for the 1 µm region and 2 µm are illustrated in Figure 24.

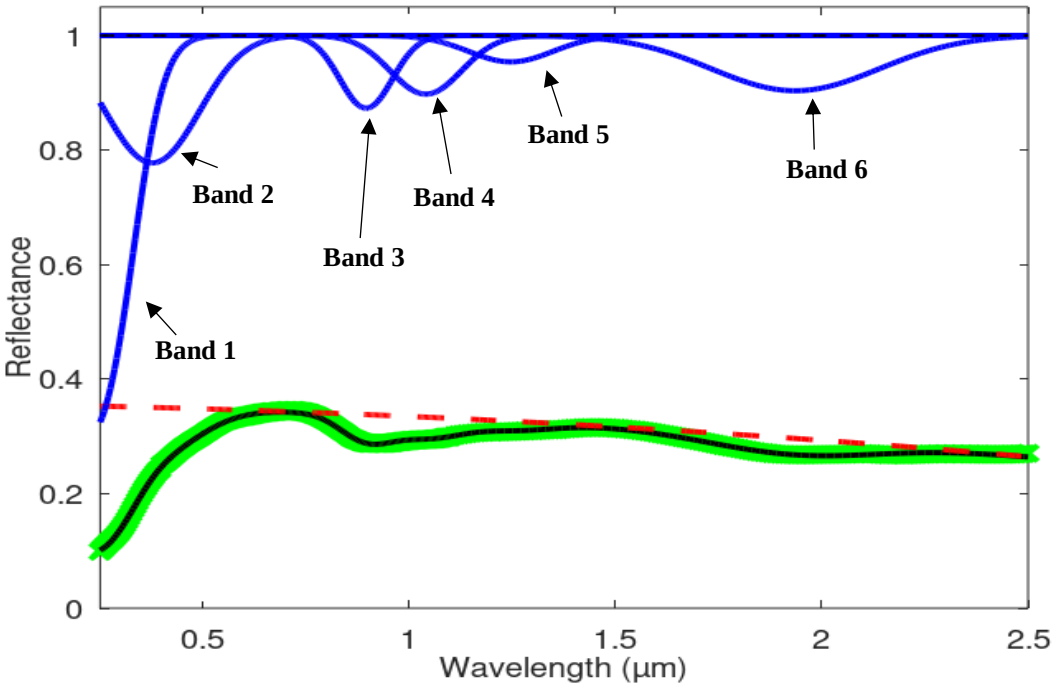


Figure 19. MGM fit for the reflectance spectra for irradiated sample of the Bjurböle. Green: reflectance spectral data, Black: MGM fit, red dash line: continuum, Bands in blue: absorption bands. Reflectance is given in logscale.

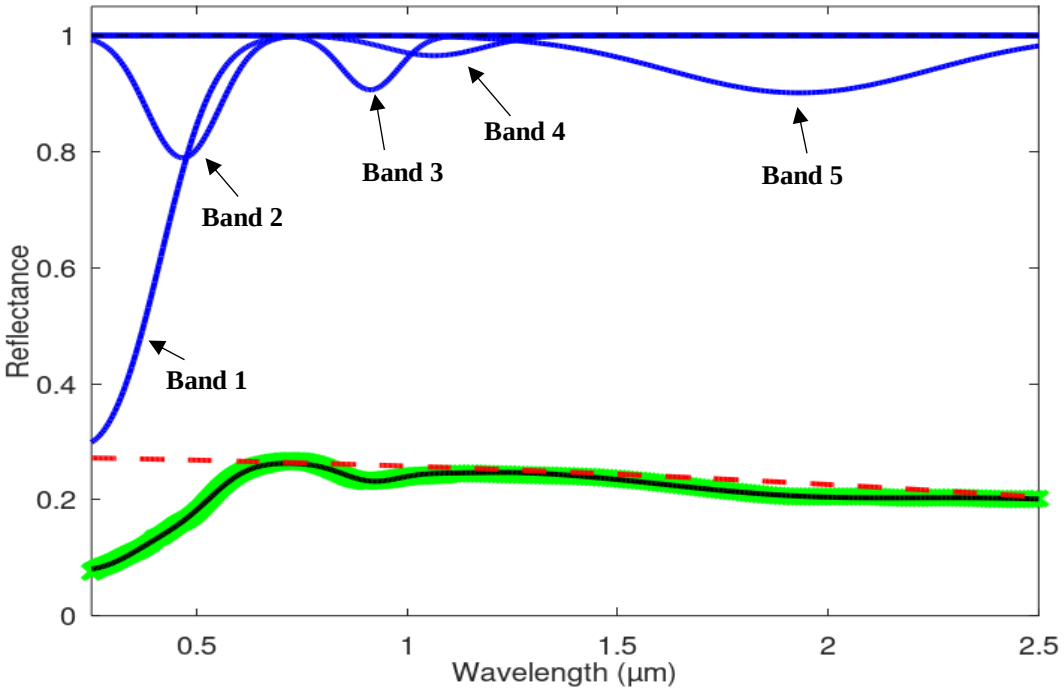


Figure 20. MGM fit for the reflectance spectra for irradiated sample of the Avanhandava. Green: reflectance spectral data, Black: MGM fit, red dash line: continuum, Bands in blue: absorption bands. Reflectance is given in logscale.

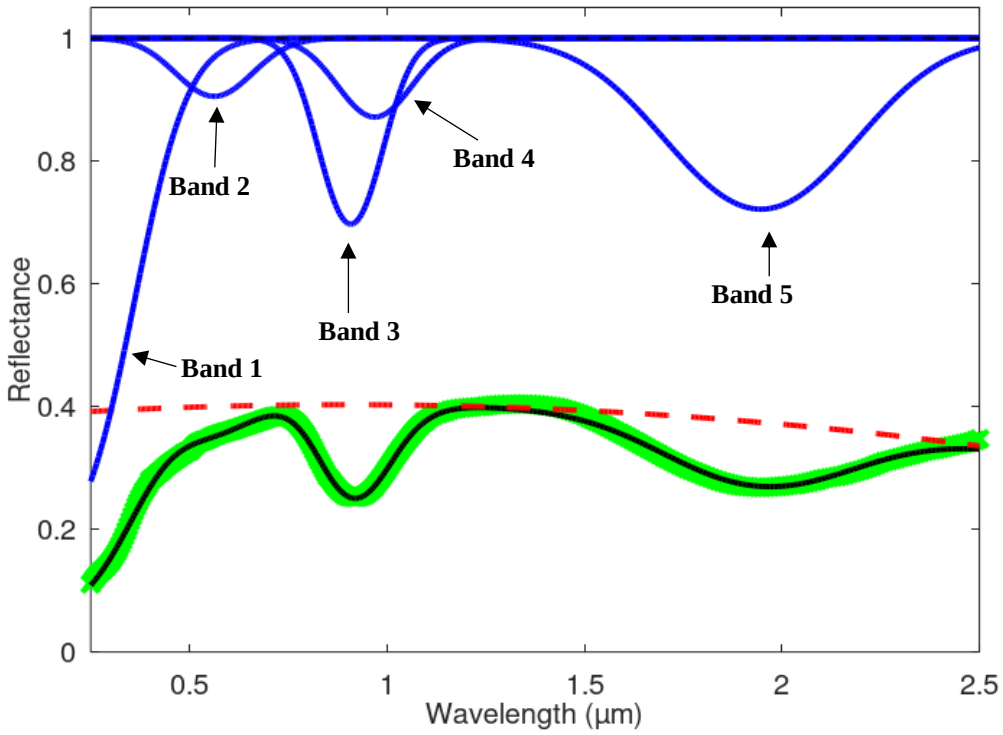


Figure 21. MGM fit for the reflectance spectra for irradiated sample of the Luotolax. Green: reflectance spectral data, Black: MGM fit, red dash line: continuum, Bands in blue: absorption bands. Reflectance is given in logscale.

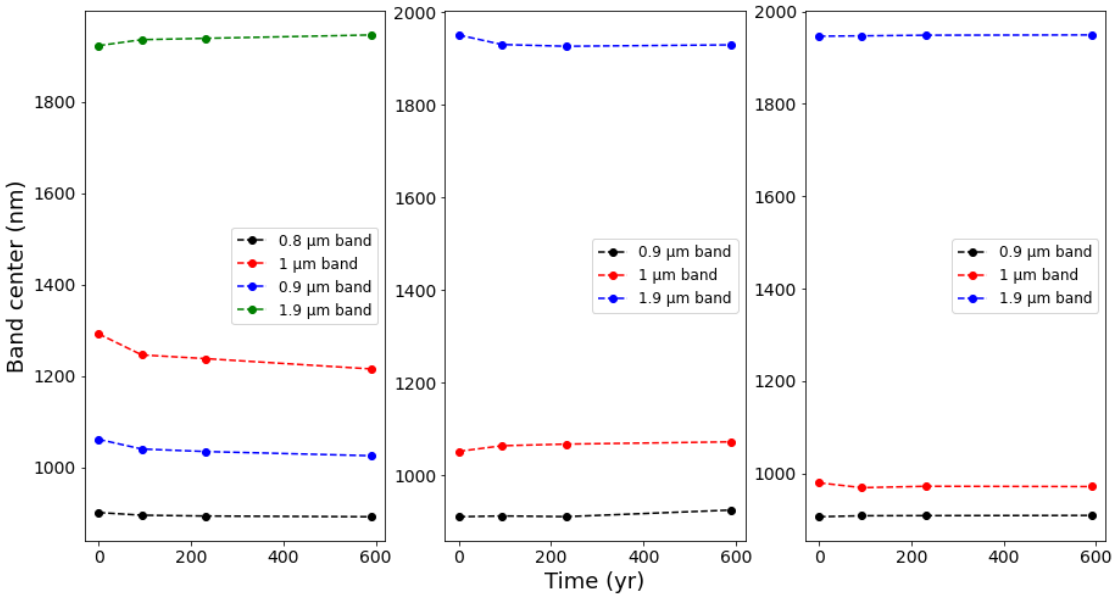


Figure 22. Each figure represents the time evolution of band center. Time, yr, was estimated for 1 au Left figure illustrates the evolution of four gaussian absorption band ceters of Bjurböle. Middle figure illustrates the evolution of three gaussian absorption bands centers of Avanhandava. Right figure illustrates evolution of three absorption band centers of Luotolax.

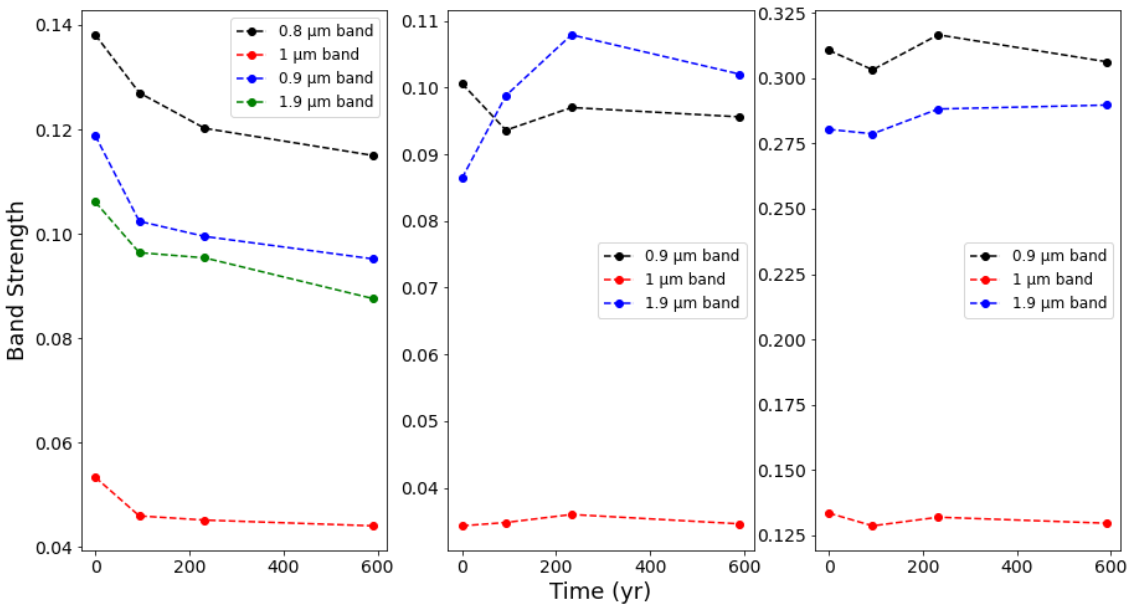


Figure 23. Each figure represents the time evolution of band strength. Time, yr, was estimated for 1 au Left figure illustrates the evolution of four gaussian absorption band ceters of Bjurböle. Middle figure illustrates the evolution of three gaussian absorption bands centers of Avanhandava. Right figure illustrates evolution of three absorption band centers of Luotolax.

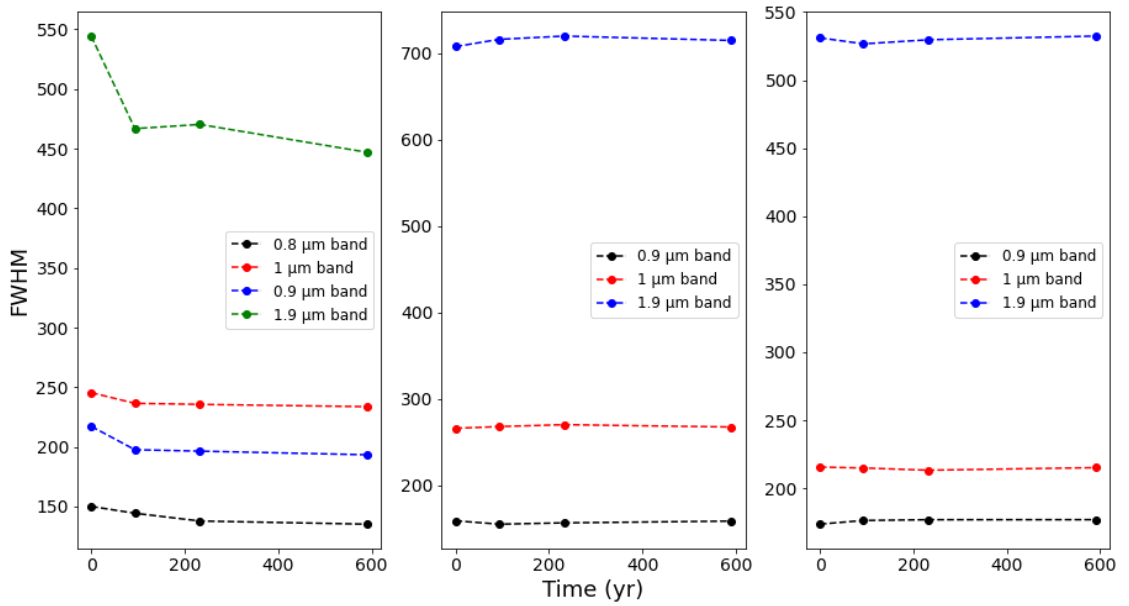


Figure 24. Each figure represents the time evolution of band FWHM. Time, yr, was estimated for 1 au Left figure illustrates the evolution of four gaussian absorption band ceters of Bjurböle. Middle figure illustrates the evolution of three gaussian absorption bands centers of Avanhandava. Right figure illustrates evolution of three absorption band centers of Luotolax.

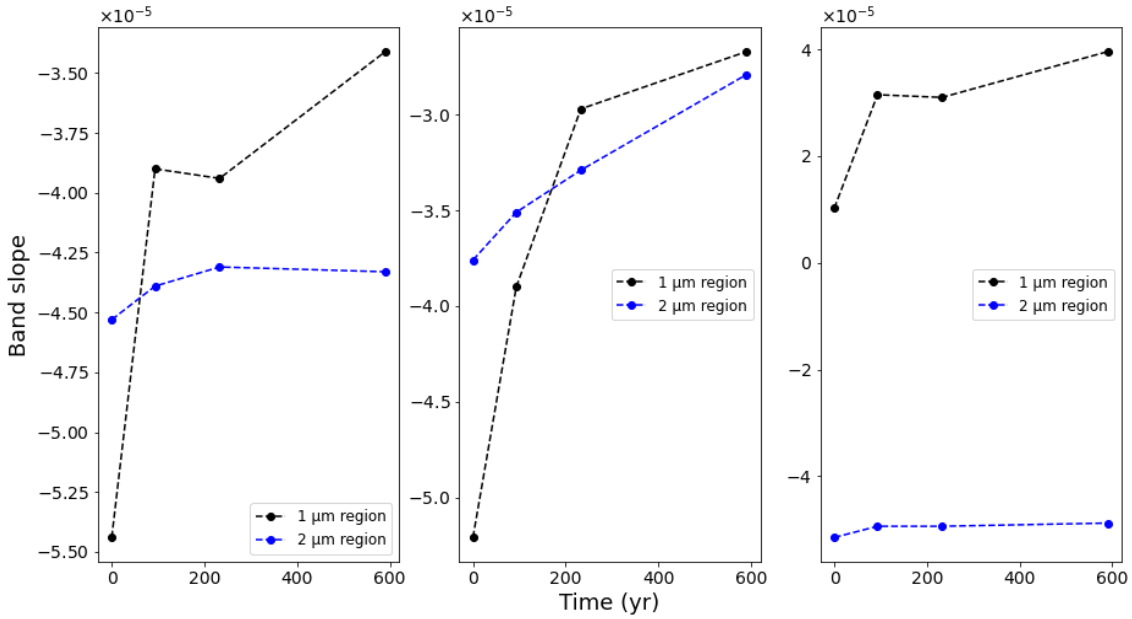


Figure 25. Each figure represents the time evolution of band slope. Time, yr, was estimated for 1 au. Figure illustrates the evolution of two absorption band ceters of Bjurböle (left), Avanhandava (middle), Luotolax (right)

Table 10. Percentage of parameter change between the fresh sample and the most exposed sample to irradiation.

| | Band center (%) | Band strength (%) | FWHM (%) | Spectral slope (%) |
|---|---|---|---|---|
| Bjurböle | | | | |
| 0.8 µm | 1.03 | 16.73 | 9.91 | |
| 0.9 µm | 5.95 | 17.42 | 4.80 | 37.32 |
| 1 µm | 3.39 | 19.87 | 10.99 | |
| 1.9 µm | 1.22 | 17.44 | 17.90 | 4.42 |
| Avanhandava | | | | |
| 0.9 µm | 1.59 | 4.97 | 0.22 | 48.75 |
| 1 µm | 1.96 | 0.87 | 0.57 | |
| 1.9 µm | 1.10 | 18.06 | 1.01 | 25.80 |
| Luotolax | | | | |
| 0.9 µm | 0.32 | 1.42 | 1.91 | 74.24 |
| 1 µm | 0.84 | 2.92 | 0.19 | |
| 1.9 µm | 0.14 | 3.32 | 0.24 | 5.24 |

# 5. DISCUSSION

## 5.1. Exposure time

As explained in the methodology, three samples of each meteorite have been irradiated under three fluences which correspond to three exposure times, ~93 years, ~230 years, and ~590 years at 1 au. Hence for OCs originated from S- and Q-type asteroids, and howardite originated from (4) Vesta, which are in the inner asteroid belt approximately at 2.3 au, the flux of the solar wind ions would be smaller, and the exposure time would be longer. The corresponding exposure time at 2.3 au for our fluences would be; ~490 years, ~1200 years, and ~3100 years, respectively. The exposure time considered in this experiment is smaller when compared to previous laboratory simulations carried out by different authors (Brunetto et al. 2005, Brunetto and Strazzulla 2005, Fulvio et al. 2012, Chrbolková et al. 2021). In this experiment, $H^+$ ions were used with low energy of 1 keV to simulate more realistic solar wind conditions. To obtain a large-scale exposure time (more than 1000 years) with 1 keV low $H^+$ ion energy requires several months of laboratory time. Hence, to obtain large-scale exposure time using low-energy ions has practical challenges.

## 5.2. Reflectance data

In Bjurböle and Avanhandava, we see a clear difference in reflectance spectra between fresh and irradiated samples (see Figure 16 and Figure 17). But in Luotolax this difference is minimum (see Figure 18). According to reflectance data, there are two major absorption bands at 1 µm (VIS region) and 2 µm (NIR region) in all samples. In Bjurböle and Avanhandava, 1 µm band is a combination of five to six overlapping absorption bands resulting from olivine and pyroxene (Burns 1970, Sunshine and Pieters 1993). Using the MGM, it was possible to separate three absorptions bands for Bjurböle at 0.8 µm, 0.9 µm, and 1 µm (Figure 18) and two absorption bands for Avanhandava at 0.9 µm and 1 µm (Figure 19). Because of the lack of resolution between these bands, it was difficult to separate all the absorption bands.

Since Luotolax is more dominated by pyroxenes, the two absorption bands resulting at 0.9 µm and 1 µm in the VIS region (Figure 20) are the result of orthopyroxene and

clinopyroxene (Sunshine and Pieters 1993). In all three meteorites, the absorption band in the NIR region is the result of pyroxenes. These results agree with the reflectance spectral studies carried out on LL, H, and howardite meteorite samples by Marchi et al. (2005), Fulvio et al. (2012), Sanchez et al. (2012).

### 5.3. Changes in band parameters

We only performed the experiment procedure once. Hence statistical error calculation could not be carried out. However, to identify trends, or if it's only noise, we compared the changes to a threshold value of 5% (Table 10). If the changes are more than 5%, it was considered as a trend. According to Figure 22, in all meteorite samples, with increasing fluences, there is minimal variation in the band center. The change in the band center in all samples was less than ~2% in both VIS and NIR regions. Sunshine and Pieters (1993) state that the band center corresponds to the mineralogy of the substance. Hence, this observation indicates that there is no change in mineralogy due to ion irradiation.

With increasing $H^+$ ion irradiation, the strength of the absorption bands of reflectance spectra of Bjurböle and Avanhandava decreases (Figure 23). For Bjurböle, this decrease is more than 15% in both VIS and NIR regions after ~590 years of exposure. The initial change in band depth is high and then gradually decreases with time, e.g., being non-linear. All the three bands in the VIS region show the same behavior. Hence, even though we could not separate all the absorption bands in this region, it can be assumed that all the unresolved bands would behave in a similar manner. For Avanhandava, the changes are less prominent compared to Bjurböle. Band strength change over increasing fluence show mixed trends or rather fluctuations. When it comes to Luotolax, band strength does not show a clear correlation with increasing fluence. The changes were less than 4% in both VIS and NIR regions.

When it comes to FWHM (Figure 24), the behavior is the same as for band depth, but the changes are less pronounced. Initially, Bjurböle shows a slight decrease in FWHM. Subsequent, the change is negligible. Avanhandava and Luotolax do not show a significant change in FWHM. In all three meteorites, the spectral slope in VIS tends to increase (reddening) significantly. In NIR region, Avanhandava shows significant reddening, Bjurböle moderate. Initial reddening of Luotolax fresh and lowest irradiated

sample in VIS region is ~60%, but further slope change as irradiation increases in subsequently smaller (~20%). The change of slope in the VIS region was greater than in the NIR region (Figure 25).

In other words, the overall results of Bjurböle show that the continuum becomes redder and absorption bands become weaker. Similar observations were made by Chrbolková et al. (2021) when simulating solar wind irradiation on olivine pellets. Avanhandava is more reduced than Bjurböle (more oxidized) and has less Fa olivine. With increasing $H^+$ ion irradiation, Avanhandava shows more random fluctuations compared to Bjurböle. Both chondrites show significant reddening in the VIS region. The reddening in the NIR region is more significant in Avanhandava than in Bjurböle. This indicates that even for low energy solar wind conditions, the chondritic materials (S- and Q- type asteroids) with high olivine content and/or higher Fa composition are more susceptible to a reduction of diagnostic silicate absorption bands and spectral reddening. The difference in NIR spectral slope is not clear.

Luotolax meteorite being howardite which is equivalent to V-type spectrum (rich in orthopyroxene and clinopyroxene) shows major VIS reddening but not observable band depth changes with increasing exposure to $H^+$ ion irradiation. Quadery et al. (2015) and Chrbolková et al. (2021) explained that the smaller band depth change in Luotolax may be due to higher pyroxene resistance to low energy ion irradiation. It is evident that VIS slope reddening is the more dominant factor at short timescale and typical solar wind energies than NIR slope in all three material compositions.

## 5.4. Comparison with previous studies and application in solar research

### *5.4.1. S- and Q- type asteroids*

Only very few research works have been carried out to study solar wind irradiation on OCs meteorite samples. Brunetto et al. (2005) performed 60 keV $Ar^{++}$ ion irradiation on Epinal (H5) OC. This study has exhibited progressive reddening that can be observed in S-type near-Earth asteroids. In our study, Avanhandava (H6) exhibits more reddening in VIS rather than in the NIR region. Furthermore, from the $H^+$ (with 5 keV), $He^+$ (with 20 keV), and $Ar^+$ (40 keV) ion irradiation carried out by Chrbolková et al. (2021) on

olivine and pyroxene samples, it is suggested that olivine-rich asteroids (e.g., S- and Q-type asteroids), may face significant and rapid changes. Additionally, the authors pointed out that this is because olivine does not have the ability to heal its defects in crystalline structure (Quadery et al. 2015). These findings complement with our results. Vernazza et al. (2009) state that compared to S-types, the Q-type asteroids exhibit less reddening and higher albedos because of their rejuvenated, fresh surface. According to the findings of this work, reddening should be observed, especially in VIS region, even on young surfaces.

Based on our findings, it can be predicted that on S- and Q- type asteroids, spectral reddening due to typical solar wind irradiation in short time scale/relatively young surfaces will be dominated in VIS region than in NIR region. Also, chondritic materials with high olivine content will show more reduction of diagnostic silicate absorption bands and spectral reddening even in a short time period (less than 1000 years). This effect will get reduced as the olivine content decreases.

*5.4.2. V-type asteroids*

Fulvio et al. (2012) have carried out ion irradiation on eucrite samples using $Ar^+$ and $C^+$ ions with energies from 60 to 200 keV. They observed progressing reddening and darkening of the irradiated samples. This was not observed in our samples. They also observed different reddening behavior between different HEDs, which may have resulted from variations in chemical composition, presence of crystals, crystal structures, or surface textures.

Reflectance spectra of asteroid (4) Vesta, as observed by the DAWN mission, indicate a fresh surface with deep absorption bands and a lack in continuum change. Studies carried out by Pieters et al. (2012) conclude that this is due to the small-scale mixing of diverse surface components. Vernazza et al. (2006) claim that this is due to the surface of (4) Vesta being protected from the solar wind by a magnetic field. Our ion irradiation experiment on Luotolax also shows less prominent reddening (less slope change) compared to OCs, and little change in absorption bands even without a magnetic field shielding or without contamination by carbonaceous material. This indicates that the properties of reflectance spectra of (4) Vesta mentioned above can be rather due to the

ability of pyroxenes to heal radiation damage caused by the solar wind (Quadery et al. 2015) and thus show little spectral change compared to olivine. Also, this study shows that unlike in S- and Q-type asteroids, V-type asteroids will not show a significant change due to solar wind irradiation in absorption band parameters in a short time scale/on relatively young surfaces.

## 6. CONCLUSIONS

$H^+$ ion irradiation with 1 keV energy was carried out under three different fluences to simulate the solar wind irradiation effect on meteorite samples. Three different meteorites were selected for the experiment, namely Bjurböle, Avanhandava, and Luotolax. Significant reddening of both chondrites in the VIS region and more significant reddening in the NIR region of Avahandava than in Bjurböle indicates that even for low energy solar wind conditions, the chondritic materials (Q/S-type asteroids) with high olivine content and/or higher Fa compositions are susceptible to early space weathering. Further, we observed band depth reduction in Bjurböle. Hence, it can be predicted that S- and Q- type asteroids' spectral reddening due to typical solar wind irradiation in short time scale/relatively young surfaces will be dominated in VIS region than in NIR region. They will show these features even in a short time period (less than 1000 years). The difference in NIR slope behavior is not clear; it may be related to the oxidation state (Avahandava being H6 and is more reduced than Bjurböle). Luotolax shows VIS reddening but no observable band depth changes nor NIR slope change with increasing exposure to $H^+$ ion irradiation to a certain extent. This is consistent with DAWN observations of asteroid (4) Vesta. The smaller change in Luotolax may be due to higher pyroxene resistance to spectral change.

My results imply that, at short timescales and typical solar wind energies, VIS slope reddening is the most dominant factor in all three materials. Also, this study shows that unlike in S- and Q-type asteroids, V-type asteroids will not show a significant change due to solar wind irradiation in absorption band parameters in a short time scale/on relatively young surfaces. This will help us to understand hyperspectral observations by space missions such as the ESA Hera/Milani mission to binary asteroid Didymos, ESA BepiColombo to Mercury, or ESA Comet Interceptor to fresh comets.

## 7. ACKNOWLEDGMENTS

I would like to take this opportunity to thank my colleges. I wish to thank my supervisor, Tomáš Kohout, and co-supervisor, Kateřina Chrbolková for their valuable guidance and support. Arto Luttinen for supporting us with meteorite samples. David Korda for his guidance with MGM fits, Kenichiro Mizohata for conducting the ion irradiation at the University Helsinki accelerator laboratory, Ilmo Kukkonen for his valuable guidance and to Antti Penttilä for the valuable guidance with reflectance spectrometer.

I also like to extend my thanks to my family, for giving the support specially my parents and my husband. Furthermore I would like to thank everyone who have encouraged me to pursue my research work in this filed.

## 8. REFERENCES


Adams, J.B. 1974. Visible and near-infrared diffuse reflectance spectra of pyroxene as applied to remote sensing of solid objects in the solar system. Journal of Geophysical Research 79, 4829-4836.

Adams, J.B. 1975. Interpretation of visible and near-infrared diffuse reflectance spectra of pyroxenes and other rock forming minerals. Academic, San Diego Califonia pp.

Ahrens, L.H. and Danchin, R.V. 1971. The chemical composition of the basaltic achondrites. Physics and Chemistry of the Earth 8, 267-303.

Bell, J.F. 1995a. Do ordinary chondrites come from S-class asteroids? Invited talk. AAS Div. for Planetary Sciences, annual meeting, Kona, Hawai'i.

Bell, J.F. 1995b. Q-class asteroids and ordinary chondrites. Lunar and Planetary Science 26, 93-94.

Bennett, C.J., Pirim, C. and Orlando, T.M. 2013. Space-weathering of solar system bodies: a laboratory perspective. Chem Rev 113, 9086-9150.

Binzel, R.P., Rivkin, A.S., Stuart, J.S., Harris, A.W., Bus, S.J. and Burbine, T.H. 2004. Observed spectral properties of near-Earth objects: results for population distribution, source regions, and space weathering processes. Icarus 170, 259-294.

Binzel, R. P., Morbidelli, A., Merouane, S., DeMeo, F. E., Birlan, M., Vernazza, P., Tomas, C. A., Rivkin, A. S., Bus, S. J., Tokunaga, A.T. 2010. Earth encounters as the origin of fresh surfaces on near-Earth asteroids. Nature 463, 331-334.

Binzel, R.P., DeMeo, F.E., Turtelboom, E.V., Bus, S.J., Tokunaga, A., Burbine, T.H., Lantz, C., Polishook, D., Carry, B., Morbidelli, A., Birlan, M., Vernazza, P., Burt, B.J., Moskovitz, N., Slivan, S.M., Thomas, C.A., Rivkin, A.S., Hicks, M.D., Dunn, T., Reddy, V., Sanchez, J.A., Granvik, M. and Kohout, T. 2019. Compositional distributions and evolutionary processes for the near-Earth object population: Results from the MIT-Hawaii Near-Earth Object Spectroscopic Survey (MITHNEOS). Icarus 324, 41-76.

Britt, D., Tholen, D.J., Bell, J.F. and M., P.C. 1992. Comparison of asteroid and meteorite spectra: Classification by principal components analysis. Icarus 99, 153-166.

Brunetto, R., Orofino, V. and Srazzulla, G. 2005. Space weathering on minor bodies induced by ion irradiaiton: some experimental results. Mem. S. A. It. 6, 45-50.

Brunetto, R. and Strazzulla, G. 2005. Elastic collisions in ion irradiation experiments: A mechanism for space weathering of silicates. Icarus 179, 265-273.

Brunetto, R., Lantz, C., Ledu, D., Baklouti, D., Barucci, M.A., Beck, P., Delauche, L., Dionnet, Z., Dumas, P., Duprat, J., Engrand, C., Jamme, F., Oudayer, P., Quirico, E., Sandt, C. and Dartois, E. 2014. Ion irradiation of Allende meteorite probed by visible, IR, and Raman spectroscopies. Icarus 237, 278-292.

Burbine, T.H., Buchanan, P.C., Dolkar, T. and Binzel, R.P. 2009. Pyroxene mineralogies of near-Earth vestoids. Meteoritics & Planetary Science 44, 1331-1341.

Burns, R.G. 1970. Mineralogical applications to crystal field theory. Cambridge University Press, New York, 224 pp.

Chapman, C.R. 1996. S-type asteroids, ordinary chondrites, and space weathering: The evidence from Galileo's fly-bys of Gaspra and Ida. meteorites & Planetary Sciences 31, 699-725.

Chrbolková, K., Brunetto, R., Ďurech, J., Kohout, T., Mizohata, K., Malý, P., Dědič, V., Lantz, C., Penttilä, A., Trojánek, F. and Maturilli, A. 2021a. Comparison of space weathering spectral changes induced by solar wind and micrometeoroid impacts using

ion- and femtosecond-laser-irradiated olivine and pyroxene. Astronomy & Astrophysics 654.

Chrbolková, K., Brunetto, R., Ďurech, J., Kohout, T., Mizohata, K., Malý, P., Dědič, V., Lantz, C., Penttilä, A., Trojánek, F. and Maturilli, A. 2021b. Comparison of space weathering spectral changes induced by solar wind and micrometeoroid impacts using ion- and femtosecond-laser-irradiated olivine and pyroxene. Astronomy & Astrophysics.

Chrbolková, K.R., Brunetto, R., Durech, J., Kohout, T., Mizohata, K., Malý, P., Václav, D., Lantz, C., Penttilä, A., Trojánek, F. and Maturilli, A. 2021c. Comparison of space weathering spectral changes induced by solar wind and micrometeoroid impacts using ion- and femtosecond laser-irradiated olivine and pyroxene. 14.

Clark, B., Hapke, B., Pieters, C. and Britt, D. 2002. Asteroid Space Weathering and Regolith Evolution. Asteroids III.

Clark, R.N. and Roush, T.L. 1984. Reflectance spectroscopy: Quantitative analysis techniques for remote sensing applications. Journal of Geophysical Research 89, 6329-6340.

Clénet, H., Pinet, P., Daydou, Y., Heuripeau, F., Rosemberg, C., Baratoux, D. and Chevrel, S. 2011. A new systematic approach using the Modified Gaussian Model: Insight for the characterization of chemical composition of olivines, pyroxenes and olivine–pyroxene mixtures. Icarus 213, 404-422.

Cloutis, R.N. and Gaffey, M.J. 1991. Pyroxene spectroscopy revisited: Spectral-compostional corrections and relationships to geothermometry. Journal of Geophysical Research 96, 809-826.

Consolmagno, G.J. and Drake, M.J. 1977. Composition and evolution of the eucrite parent body: evidence from rare earth elements. Geochimica et Cosmochimica Acta 41, 1271-1282.

Crandall, P.B. 2018. Simulated space weathering of planetary surfaces. Masters of Science in Chemisrty Graduate Department, pp. available at.

Crawford, M. 2008. Meteorites pictured: Campo del Cielo, Pallasovka, NWA 4473, NWA 5018.

DeMeo, F.E., Binzel, R.P., Slivan, S.M. and Bus, S.J. 2009. An extension of the Bus asteroid taxonomy into the near-infrared. Icarus 202, 160-180.

Dodd, R.T., Schmus, W.R.V. and Koffman, D.M. 1967. A survey of the unequilibrated ordinary chondrites. Geochimica et Cosmochimica Acta 31, 921-951.

Duffard, R., Lazzaro, D., Licandro, J., De Sanctis, M.C. and Capria, M.T. 2006. V-type asteroids: A mineralogical study. Advances in Space Research 38, 1987-1990.

Fazio, A., Harries, D., Matthäus, G., Mutschke, H., Nolte, S. and Langenhorst, F. 2017. Femtosecond laser irradiation of olivine single crystals: Experimental simulation of space weathering. Icarus 299.

Fernandez, Y.R., Howell, J.-Y.L. and Woodey, L.M. 2015. Asteroids and Comets. Treatise on Geophysics 10, 487-528.

Fulvio, D., Brunetto, R., Vernazza, P. and Strazzulla, G. 2012. Space weathering of Vesta and V-type asteroids: new irrediation experiments on HED meteorites Astronomy & Astrophysics 537, 5.

Gaffey, M.J., Bell, J.F., Brown, R.H., Burbine, T.H., Piatek, J.L., Reed, K.L. and Chaky, D.A. 1993. Mineralogical Variations within the S-Type Asteroid Class. Icarus 106, 573-602.

Gosling, J.T. 2007. The solar wind, in Encyclopedia of Solar System. Acadamic, Amsterdam.

Han, H., Lu, X., Yang, Y., Zhang, H. and Mutelo, A.M. 2020. Study of the Modified Gaussian Model on olivine diagnostic spectral features and its applications in space weathering experiments. Research in Astronomy and Astrophysics, 1-27.

Hanzen, R.M., Bell, P.M., and Mao, H.K. 1978. Effects of compositional variation on absorption spectra of lunar pyroxenes Proc. Lunar Planets Science Conference 9, 2919-2934.

Hapke, B. 1973. Darkening of silicate rock powders by solar wind sputtering. The moon 7, 342-355.

Hapke, B. 2001. Space weathering from Mercury to the asteroid belt. Journal of Geophysical Research 106, 10039-10073.

Hiroi, T., Pieters, C.M. and Takeda, H. 1994. Grain size of the surface of asteroid 4 Vesta estimated from its reflectance spectrum in comparison with HED meteorites. Meteoritics & Planetary Science 29, 394-396.

Hu, S. and Lin, Y. 2012. Space weathering simulation and spectrum decoding. Chinese Journal of Geochemistry 31, 128-135.

Hughes, D.W. 1977. A Disaggregation and Thin Section Analysis of the Size and Mass Distribution of the Chondrules in the Bjurböle and Chainpur Meteorites Earth and Planetary Science Letters 38, 391-400.

Huss, G., Rubin, A. and Grossman, J. 2006. Thermal Metamorphism in Chondrites. Meteorites and the Early Solar System II.

Kallemeyn, G.W., Rubin, A.E., Wang, D., and Wasson, J.T. 1989. Ordinary chondrites: Bulk compositions, classification, lithophile-element fractionations, and composition-petrographic type relationships. Geochimica et Cosmochimica Acta 53, 2747-2767.

Kallemeyn, G.W. 1996. The classificational wanderings of the Ningqiang chondrite. Lunar and Planetary Science 27, 635-636.

Kohout, T., Gritsevich, M., Grokhovsky, V.I., Yakovlev, G.A., Haloda, J., Halodova, P., Michallik, R.M., Penttilä, A. and Muinonen, K. 2014. Mineralogy, reflectance spectra, and physical properties of the Chelyabinsk LL5 chondrite – Insight into shock-induced changes in asteroid regoliths. Icarus 228, 78-85.

Kovach, H.A. and Jones, R.H. 2010. Feldspar in type 4-6 ordinary chondrites: Metamorphic processing on the H and LL chondrite parent bodies. Meteoritics & Planetary Science 45, 246-264.

Kuhlman, K.R., Sridharan, K. and Kvit, A. 2015. Simulation of solar wind space weathering in orthopyroxene. Planetary and Space Science 115, 110-114.

Lewis, J.A., and Jones, R.H. 2022. Exsolution in alkali feldspar in ordinary chondrites: Ubiquitous evidence for rapid cooling at high temperatures. Geochimica et Cosmochimica Acta 321, 293-310.

Loeffler, M.J., Dukes, C.A. and Baragiola, R.A. 2009. Irradiation of olivine by 4 keV He+: Simulation of space weathering by the solar wind. Journal of Geophysical Research 114.

MacLennan, E.M., Emery, J.P. and Lindsay, S.S. 2017. Space weathering of silicae asteroids: an observational investigation. American Astronomical Society, DPS meeting 49.

Maksimova, A.A., Petrova, E.V., Chukin, A.V., Nogueira, B.A., Fausto, R., Szabo, A., Dankhazi, Z., Felner, I., Gritsevich, M., Kohout, T., Kuzmann, E., Homonnay, Z. and Oshtrakh, M.I. 2021. Bjurbole L/LL4 ordinary chondrite properties studied by Raman spectroscopy, X-ray diffraction, magnetization measurements and Mossbauer spectroscopy. Spectrochim Acta A Mol Biomol Spectrosc 248, 119196.

Marchi, S., Brunetto, R., Magrin, S., Lazzarin, M. and Gandolfi, D. 2005. Space weathering of near-Earth and main belt silicate-rich asteroids: observations and ion irradiation experiments. Astronomy & Astrophysics 443, 769-775.

Marfunin, A.S. 1979. Minerals and inorganic materials Springer-Verlag, New York, 340 pp.

Mason, B. 1967. Meteorites. Am. Sci. 55, 429-455.

Matson, D., Johnson, T. and Veeder, G. 1977. Soil maturity and planetary regoliths: The Moon, Mercury and the asteroids. Proc. Lunar Planets Science Conference 8, 1001-1011.

McCord, T.B., Adams, J.B. and Johnson, T.V. 1970. Asteroid Vesta: Spectral Reflectivity and Compositional Implications. Science 168, 1445.

McCord, T.B. and Johnson, T.V. 1970. Lunar spectral reflectivity (0.30 to 2.50 microns) and implications for remote mineralogical analysis. Science 168, 1445.

McCord, T.B. and Adams, J.B. 1973. Progress in remote optical analysis of lunar surface composition. Moon 7, 453-474.

McSween, H.Y., Binzel, R.P., De Sanctis, M.C., Ammannito, E., Prettyman, T.H., Beck, A.W., Reddy, V., Le Corre, L., Gaffey, M.J., McCord, T.B., Raymond, C.A. and Russell, C.T. 2013. Dawn; the Vesta-HED connection; and the geologic context for eucrites, diogenites, and howardites. Meteoritics & Planetary Science 48, 2090-2104.

Meteoritical.Bulletin.Database 2022, "Meteoritical Bulletin Database ". https://www.lpi.usra.edu/meteor/metbull.php.

MIT 2016, "Asteroid Mining." https://web.mit.edu/12.000/www/m2016/finalwebsite/solutions/asteroids.html.

Nakamura, T., Noguchi, T., Tanaka, M., Zolensky Michael, E., Kimura, M., Tsuchiyama, A., Nakato, A., Ogami, T., Ishida, H., Uesugi, M., Yada, T., Shirai, K., Fujimura, A., Okazaki, R., Sandford Scott, A., Ishibashi, Y., Abe, M., Okada, T., Ueno, M., Mukai, T., Yoshikawa, M. and Kawaguchi, J. 2011. Itokawa Dust Particles: A Direct Link Between S-Type Asteroids and Ordinary Chondrites. Science 333, 1113-1116.

NASA 19.12.2019. "Meteors & Meteorites " NASA, Science: Solar System Exploration., .https://solarsystem.nasa.gov/asteroids-comets-and-meteors/meteors-and-meteorites/in-depth/.

Pfalzner, S., Davies, M., Gounelle, M., Johansen, A., Muenker, C., Lacerda, P., Portegies Zwart, S., Testi, L., Trieloff, M. and Veras, D. 2015. The formation of the solar system. Physica Scripta 90.

Pieters, C.M., Fischer, E.M., Rode, O. and Basu, A. 1993. Optical effects of space weathering: The role of the finest fraction. Journal of Geophysical Research: Planets 98 (E11), 20817-20824.

Pieters, C.M., Taylor, L.A., Noble, S.K., Keller, L.P., Hapke, B., Morris, R.V., Allen, C.C., Mckay, D.S. and Wentworth, S. 2000. Space weathering on airless bodies: Resolving a mystry with lunar samples. Meteoritics & Planetary Science 35, 1101-1107.

Pieters, C.M., Ammannito, E., Blewett, D.T., Denevi, B.W., De Sanctis, M.C., Gaffey, M.J., Le Corre, L., Li, J.Y., Marchi, S., McCord, T.B., McFadden, L.A., Mittlefehldt, D.W., Nathues, A., Palmer, E., Reddy, V., Raymond, C.A. and Russell, C.T. 2012. Distinctive space weathering on Vesta from regolith mixing processes. Nature 491, 79-82.

Pieters, C.M. and Noble, S.K. 2016. Space Weathering on Airless Bodies. J Geophys Res Planets 121, 1865-1884.

Prior, G.T. 1920. The classification of meteorites. Mineral. Mag. 19, 51-63.

Quadery, A.H., Pacheco, S., Au, A., Rizzacasa, N., Nichols, J., Le, T., Glasscock, C. and Schelling, P.K. 2015. Atomic-scale simulation of space weathering in olivine and orthopyroxene. Journal of Geophysical Research: Planets 120, 643-661.

Reddy, V., Dunn, T.L., Thomas, C.A., Moskovitz, N.A. and Burbine, T.H. 2015. Mineralogy and surface composition of asteroids. Earth and Plnetary Astrophysics.

Roush, T.L. and Singer, R.B. 1986. Gaussian analysis of temperature effects on the reflectance spectra of mafic minerals in the 1-μm region. Journal of Geophysical Research 91, 10301-10308.

Sanchez, J.A., Reddy, V., Nathues, A., Cloutis, E.A., Mann, P. and Hiesinger, H. 2012. Phase reddening on near-Earth asteroids: Implications for mineralogical analysis, space weathering and taxonomic classification. Icarus 220, 36-50.

Sasaki, S., Nakamura, K., Hamabe, Y., Kurahashi, E. and Hiroi, T. 2001. Production of iron nanoparticles by laser irradiation in a simulation of lunar-like space weathering. Nature 410, 555-557.

Sasaki, S., Kurahashi, E., Yamanaka, C. and Nakamura, K. 2003. Laboratory simulation of space weathering: Changes of optical properties and TEM/ESR confirmation of nanophase metallic iron. Advances in Space Research 31, 2537-2542.

Schwenn, R. 2000. Solar Wind: Global Properties.In: (Eds). The Encyclopedia of Astronomy and Astrophysics,Volume.

Singer, R.B. 1981. Near-infrared spectral reflectance of mineral mixtures: Syetematic combinations of pyroxenes, olivine, and iron oxides. Journal of Geophysical Research 86, 7967-7982.

Smith, G. and Strens, R.G.J. 1976. Intervalence-transfer absorption in some silicate, oxide and phosphate minerals. John Wiley, New York pp.

Stöffler, D., Hamann, C. and Metzler, K. 2018. Shock metamorphism of planetary silicate rocks and sediments: Proposal for an updated classification system. Meteoritics & Planetary Science 53, 5-49.

Stöffler, D., Hamann, C. and Metzler, K. 2019. Addendum to "Stöffler, D., Hamann, C., and Metzler, K., Shock metamorphism of planetary silicate rocks and sediments: Proposal for an updated classification system. Meteoritics & Planetary Science 53, 5–49, 2018". Meteoritics & Planetary Science 54, 946-949.

Sunshine, J. and Pieters, C. 1993. Estimating modal abundances from the spectra of natural and laboratory pyroxene mixtures using the modified gaussian model. Journal of Geophysical Research 98, 9075-9087.

Sunshine, J.M., Pieters, C.M. and Pratt, S.F. 1990. Deconvolution of mineral absorption bands: An improved approach. Journal of Geophysical Research 95.

Tachibana, S., Abe, M., Arakawa, M., Fujimoto, M., Iijima, Y., Ishiguro, M., Kitazato, K., Kobayashi, N., Namiki, N., Okada, T., Okazaki, R., Sawada, H., Sugita, S., Takano, Y., Tanaka, S., Watanabe, S., Yoshikawa, M. and Kuninaka, H. 2014. Hayabusa2: Scientific importance of samples returned from C-type near-Earth asteroid (162173) 1999 JU3. Geochemical Journal 48, 571-581.

Thompson, M.S., Morris, R.V., Clemett, S.J., Loeffler, M.J., Trang, D., Keller, L.P., Christoffersen, R. and Agresti, D.G. 2020. The effect of progressive space weathering on the organic and inorganic components of a carbonaceous chondrite. Icarus 346.

Van Schmus, W.R. and Wood, J.A. 1967. A chemical-petrologic classification for the chondritic meteorites. Geochim. Cosmochim 31, 747-765.

Vernazza, P., Brunetto, R., Strazzulla, G., Fulchignoni, M., Rochette, P., Meyer-Vernet, N. and Zouganelis, I. 2006. Asteroid colors: a novel tool for magnetic field detection? The case of Vesta. Astronomy & Astrophysics 451, L43-L46.

Vernazza, P., Binzel, R.P., Rossi, A., Fulchignoni, M. and Birlan, M. 2009. Solar wind as the origin of rapid reddening of asteroid surfaces. Nature 458, 993-995.

Weisberg, M., McCoy, T. and Krot, A. 2006. Systematics and Evaluation of Meteorite Classification. Meteorites and the Early Solar System II 2, 19-52.

Williams, M.S. 2020,"Asteroid mining to shape the future of our wealth." https://interestingengineering.com/asteroid-mining-to-shape-the-future-of-our-wealth.

Yamada, M., Sasaki, S., Nagahara, H., Fujiwara, A., Hasegawa, S., Yano, H., Hiroi, T., Ohashi, H. and Otake, H. 1999. Simulation of space weathering of planet-forming materials: Nanosecond pulse laser irradiation and proton implantation on olivine and pyroxene samples. Earth, Planets and Space 51, 1255-1265.

Yeomans, D.K. 1998, "Why Study Asteroids." Solar System Dynamics. https://ssd.jpl.nasa.gov/?why_asteroids.

**9. Appendix 1**

Diagram expressing the systematics of meteorite classification and showing the major meteorite divisions, classes, clans, and groups and relationships among meteorite groups. URE — ureilite, ACA — acapulcoite, LOD — lodranite, ANG — angrite, AUB — aubrite, BRA — brachinite, WIN — winonaite, HED — howardite-eucrite-diogenite, MES — mesosiderite, MG PAL — main-group pallasite, ES PAL — Eagle Station pallasite, PP PAL — pyroxene pallasite, SHE — shergottite, NAK — nakhlite, CHA — chassignite, OPX — orthopyroxenite.